already reported in our previous publication, **1** was polymerized using (nbd)Rh$^+$ B$^-$(C_6H_5)$_4$ as the catalyst at around 25 to 50 °C in a mixed solvent of THF and water (9:1, v/v).[12] In this study, we performed the copolymerization of **1** with **5** under similar conditions. The copolymerization with various feed ratios of **1** to **5** was carried out using the Rh catalyst (5.0 mol-% for **1** + **5**) at 30 °C in a THF-water mixed solvent under argon. After polymerization, the resulting mixture was concentrated and then dissolved in DMSO. The solution was poured into a large amount of methanol to precipitate the polymeric product. The precipitate was isolated by filtration and dried under reduced pressure to give the copolymer **6** (Table 1). The copolymer was soluble in water and DMSO, and its $\overline{M}_n$ value was estimated by GPC analysis with water as eluent using pullulan standards. Figure 1a shows the ^{1}H NMR spectrum of the copolymer (entry 1, Table 1) measured in DMSO-d_6. The signals due to the sugar and alkyl protons are observed at around δ 3.0–4.3 (signals **e**–**h**) and δ 0.84, 1.21, 1.45, 2.15 (signals **a**–**d**), respectively. In addition to these signals, signal **i** ascribed to the main-chain proton of -CH=C- appears centered at δ 6.11. The chemical shift of this signal realistically corresponds to the *cis*-isomer. Furthermore, there is no signal due to the *trans*-isomer at lower magnetic field from the *cis*-signal. The NMR results support structure **6** as that of the copolymer, which is mainly composed of *cis*-isomer. The unit ratio of the copolymer is calculated by the integrated ratio of signal **a** and signal **i**.

Table 1 shows the copolymerization results obtained by the various feed ratios of **1** to **5**. The yields and the $\overline{M}_n$ values are 57.0–78.1% and 5 200–9 700, respectively. The unit ratios of **5** in the copolymers increase with increasing molar ratios of **5** in the feeds. In all cases, however, the ratios of **5** in the copolymers are lower than those in the feeds. This is probably because the copolymers with higher

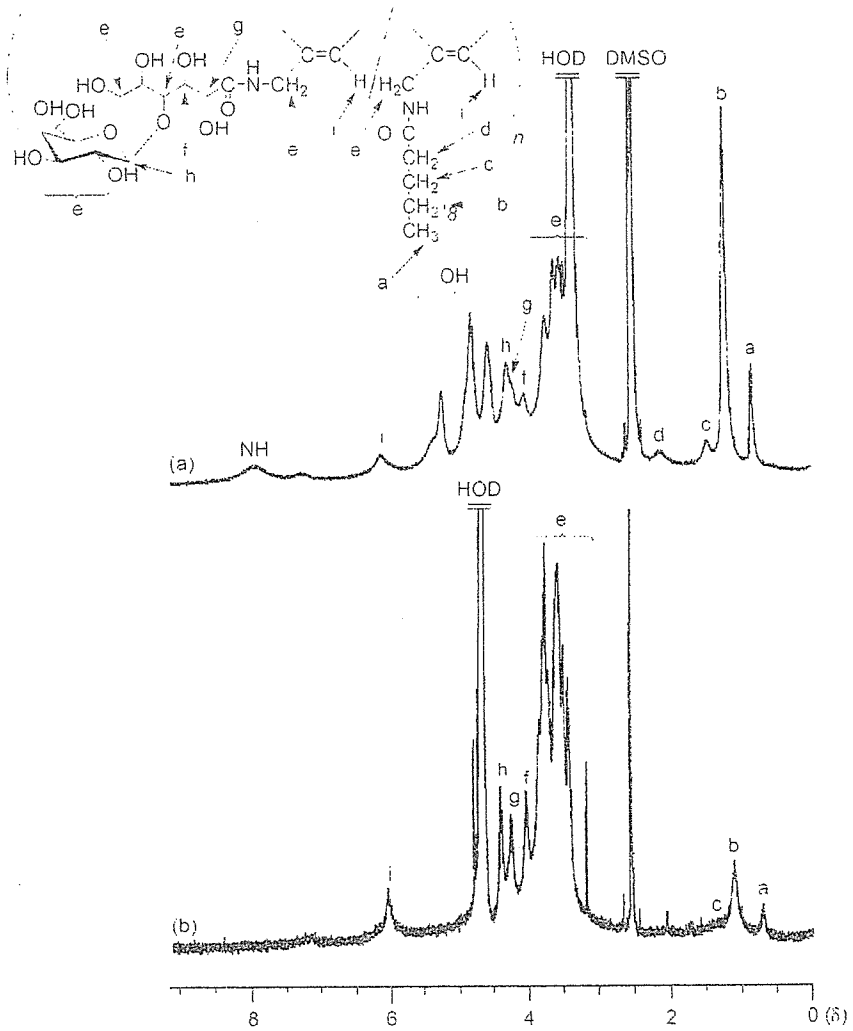

Figure 1. ^{1}H NMR spectra of copolymer **6** (entry 1, Table 1) in DMSO-d_6 (a) and D_2O (b).

contents of the unit **5** are lost as methanol-soluble fractions during the isolation procedure. The optical rotations of the copolymers with the higher contents of the sugar units were larger than those with the lower contents.

Formation of Molecular Aggregates in Water

When the copolymerization was followed by thin-layer chromatography (TLC) on silica gel (methanol: chloroform = 2:1 for **1**; hexane: ethyl acetate = 1: 1 for **5**), **1** appeared to be consumed at the early stage of the reaction; subsequently, the consumption of **3** at a later stage was confirmed. This indicated that **6** had the block copolymeric sequence between the unit **1** and the unit **5** rather than in random style. In fact, the intensities of the alkyl signals **a–d** in the ^{1}H NMR spectrum of **6** in D_2O (Figure 1b) are obviously lower than those of the same copolymer measured in DMSO-d_6 (Figure 1a). The NMR results suggest formation of micelle-like aggregates having the outer hydrophilic sugar residues and the inner hydrophobic lauryloyl groups in water, and this was attributed to the block copolymeric sequence. The formation of molecular aggregates of **6** in water was also confirmed by the GPC measurements on aqueous solutions of **6** (entry 5, Table 1, the unit ratio of **1** to **5** = 1.0:0.26) ranging in concentration from 0.05 to 9.0 mg · mL^{-1}. Figure 2 shows the relations of the $\overline{M}_n$ values to the sample concentrations in the GPC experiments. The $\overline{M}_n$ values increase from ca. 6300 to ca. 11000 for concentrations higher than 0.70 mg · mL^{-1}. These data suggest the formation of molecular aggregates for the higher concentrations of **6** in water. The molecular aggregates of **6** were directly observed by SEM. The SEM image of the spin-coated sample from the aqueous solution of **6** (entry 4, Table 1, the unit ratio of **1** to **5** = 1.0:0.32) on aluminium plate (Figure 3) shows the particle-type molecular aggregates with average diameters of 20–40 nm. The particle sizes were also confirmed by DLS measurement. The mean particle diameter of the sample shown as entry 4 in Table 1 was 85.2 ± 14.1 nm. The difference in the aggregate sizes obtained by SEM and DLS can be attributed to the difference in the sample condition: dry for SEM and wet for DLS.

Secondary Conformation of 6

We already reported in our previous report that the CD spectrum of the homopolymer **2** in water showed the positive Cotton effect at 330 nm corresponding to the main-chain UV-vis absorption.[12] This indicated the possibility for formation of a one-handed helical conformation in the main chain of **2**. In this study, the CD analysis was also performed to reveal the secondary conformation of copolymer **6**. Figure 4 shows the CD spectra of **6** (entry 5, Table 1, unit ratio of **1** to **5** = 1.0:0.26) in comparison with those of copolymer **4** (unit ratio of **1** to **3** = 1.0: 0.39) measured in DMSO and water at room temperature. The CD spectrum of **6** in DMSO (Figure 4a) shows the positive Cotton effect at 360 nm, corresponding to the main-chain UV-vis absorption. The positive Cotton effect also appeared at this region in the CD spectrum in water (Figure 4b), although its intensity was lower than that in DMSO. It has been reported that the helical structure of poly(*N*-propargylamide)s is stabilized by the intramolecular hydrogen bonds between the pendant amide groups.[17] In polar solvents such as DMSO and water, therefore, the hydrogen bonds are readily broken to effect destabilization of the helical structure. The helical conformation of **6** in polar solvents is probably stabilized by the bulky substituents in the side chains of sugar and lauryloyl groups. These bulky groups shield the hydrogen bonds from the solvents, which consequently stabilizes the helical structure. This reasoning is also supported by comparison of the CD spectra of copolymer **4** (gray lines in

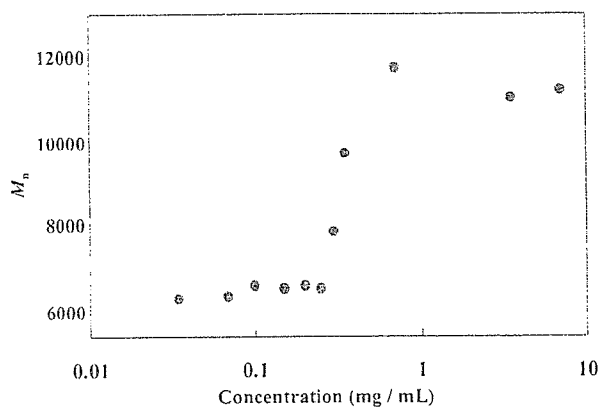

Figure 2. $\overline{M}_n$ values versus sample concentrations in GPC measurements with water as eluent (entry 5, Table 1).

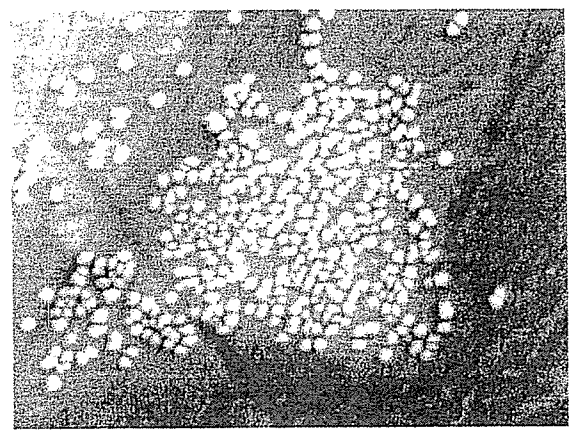

Figure 3. SEM image of **6**; the sample was prepared by spin coating of the dispersed solution of **6** (entry 4, Table 1) in water.

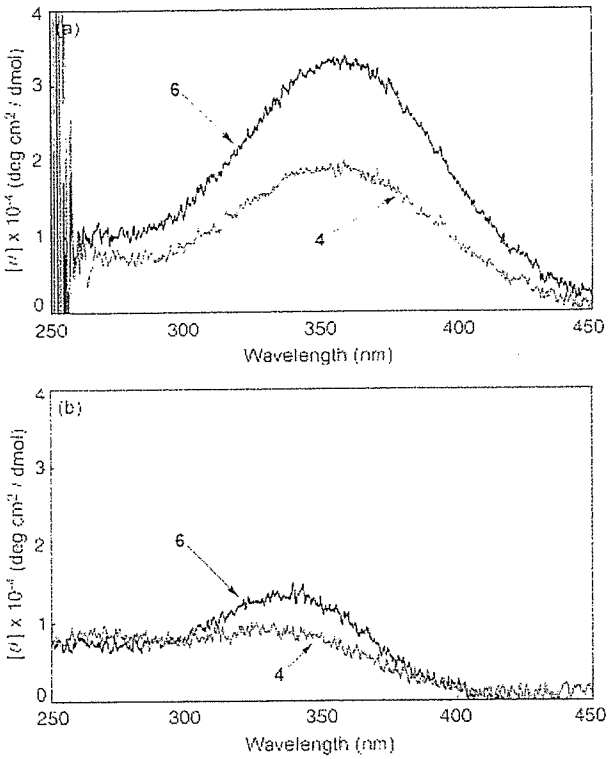

Figure 4. CD spectra of **6** (entry 5, Table 1, unit ratio: 1:5 1.0:0.26) and **4** (unit ratio: 1:3 1.0:0.39) in DMSO (a) and water (b) (c 0.2 mmol · L^{-1}).

Figure 4a, b), which has the less bulky hexanoyl groups. The CD spectra of **4** show weaker Cotton effects than those of **6**, indicating the stabilization of the helical conformation as a result of the bulkiness of the pendant groups.

Cellular Uptake of Amphiphilic Copolymer 8

To evaluate cell uptake of the copolymer by fluorescence microscopy, the rhodamine B dye moiety was introduced into the amphiphilic copolymer. First, an *N*-propargylamide derivative **7** having a pendant rhodamine B moiety was prepared by condensation of *N*-propargylamine hydrochloride with rhodamine B in the presence of a condensing agent (1-[(3-dimethylamino)propyl]-3-ethylcarbodiimide hydrochloride) in methanol. Then, the isolated **7** was copolymerized with **1** and **5** under conditions similar to those described above (Scheme 3). Although **7** did not have homopolymerizability by Rh catalyst, the unit from **7** was slightly incorporated into the resulting terpolymer by the copolymerization. The existence of the rhodamine B moiety in the obtained terpolymer **8** was confirmed by appearance of the signals due to methyl protons of N-CH_2CH_3 as well as the aromatic protons in the ^{1}H NMR spectrum of the product. However, the intensities of the signals were too weak to determine the exact content of the dye moiety in the copolymer by the integration ratio. For comparison, hydrophilic copolymer **9** was synthesized by copolymerization of monomer **1** with monomer **7** using Rh catalyst (Figure 5).

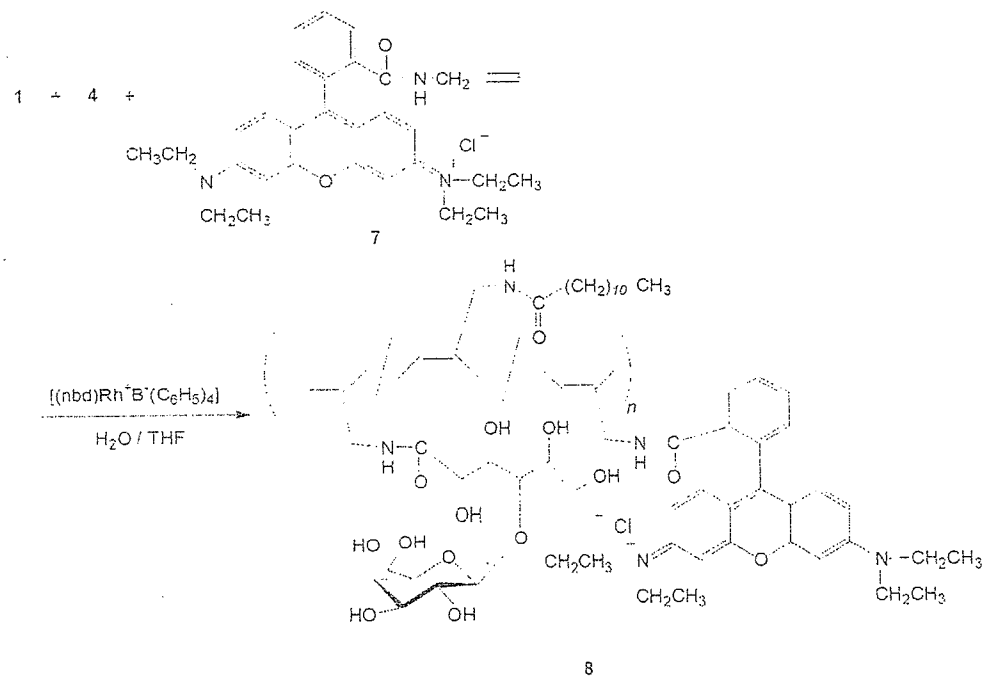

Scheme 3. Terpolymerization of **1**, **5**, and **7**.

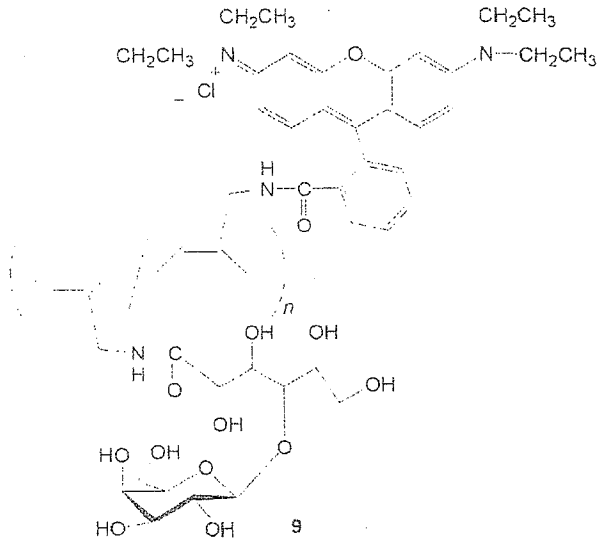

Figure 5. Structure of copolymer **9**.

The cell uptake of terpolymer **8** was studied by culturing human aortic endothelial cells (HAECs) in a culture medium containing the terpolymer **8**. Ten milligrams of **8** was suspended in 10 mL of culture medium EGM-2 and stirred for 3 h at room temperature. The suspension of **8** was sonicated at 25 W and 40 kHz for 5 min in an ultrasonic bath. The sonication was repeated twice. The obtained suspension was filtered through membrane filters with the pore sizes of 0.45 μm and 0.2 μm for sterilization. An aqueous solution of polymer **9** was prepared by following the above procedure. To evaluate the concentration of **8**, a calibration curve (data not shown) was obtained by using the aqueous solution of **9** (1 mg · mL^{-1}) as a standard polymer sample to relate concentration to fluorescence intensity. The concentration of **8** was estimated to be 0.09 mg · mL^{-1} by using the calibration curve. The DLS measurement revealed that the polymer aggregates (nanoparticles) of **8** have a mean diameter of 114.9 ± 32 nm in a culture medium containing 10% bovine serum. HAECs were exposed to the polymer aggregates of **8** while they were cultured in the culture medium containing the amphiphilic polymer **8**. After the prescribed period of culture, 1, 6, or 24 h, the HAECs were fixed in 10% formaldehyde neutral buffer solution for microscope observation. Figure 6 shows phase contrast (a), fluorescence (b), and merged (phase contrast – fluorescence) (c) images of HAECs after 24 h of incubation. The merged image demonstrates that red fluorescent light of rhodamine B was emitted from the sites where HAECs were located. This indicates that the polymer aggregates of **8** were incorporated into HAECs. The fluorescence images at each time of incubation are shown in Figure 7. The fluorescence images get brighter with the incubation time. To quantitatively evaluate cell uptake of nanoaggregates, fluorescence intensity per image (1 360 × 1 024 pixels) was determined by integrating the brightness at each pixel of the fluorescence image using image analysis software. The

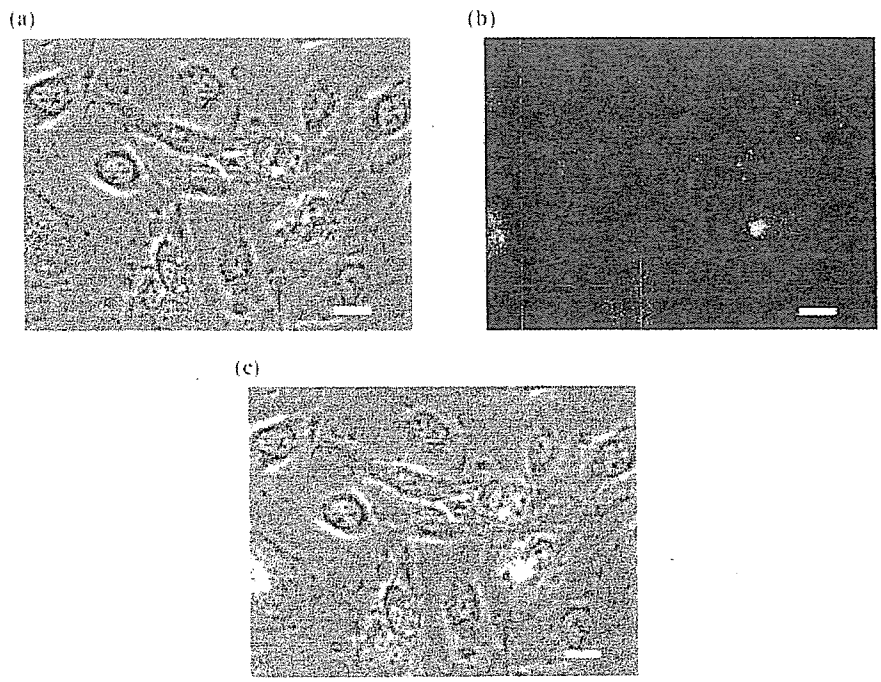

Figure 6a–c. Localization of rhodamine B-labeled copolymer **8** in human aortic endothelial cells. Phase contrast image (a), fluorescence image (b), and merged image of (a) and (b). Bars: 20 μm.

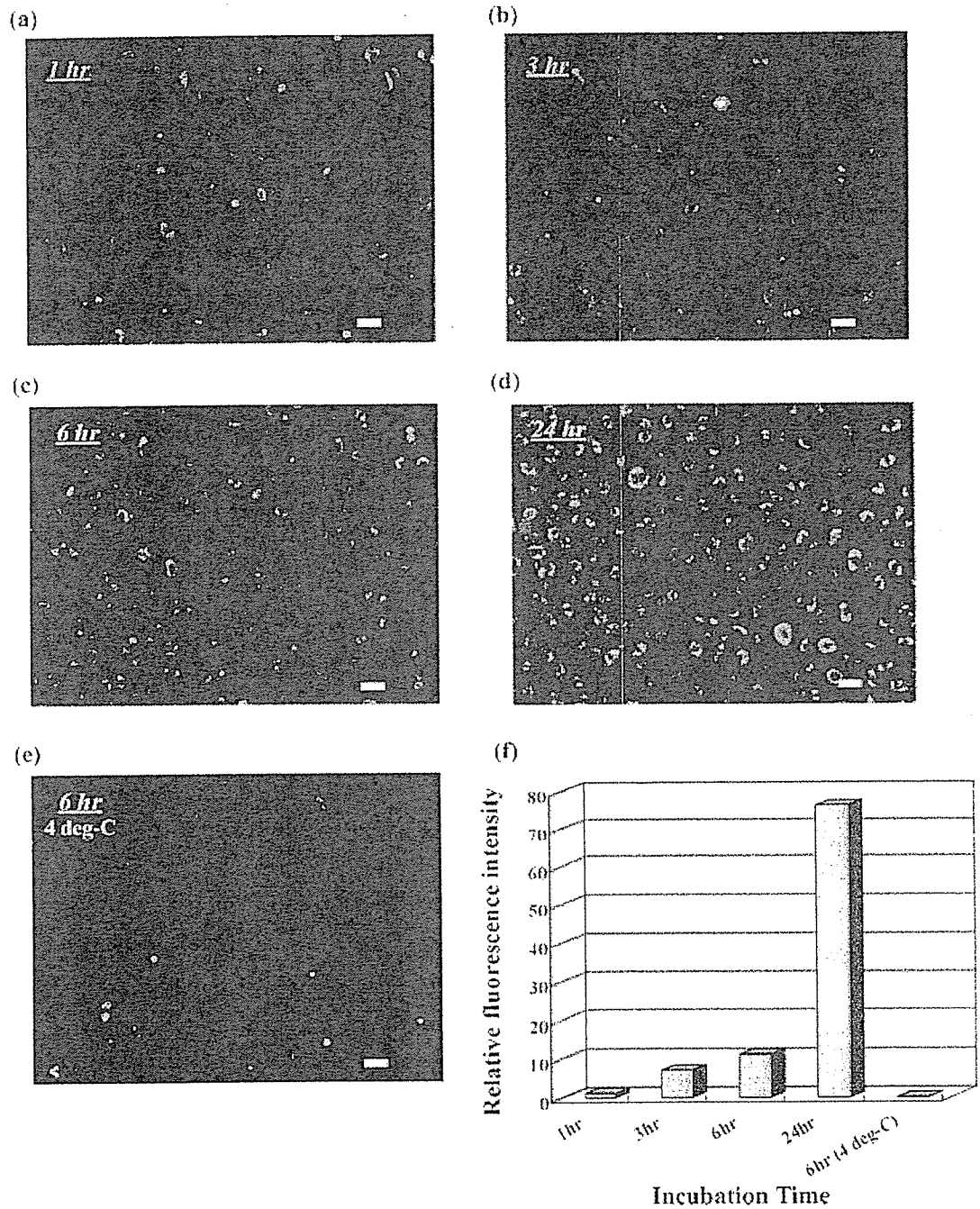

Figure 7a–f. Uptake of rhodamine B-labeled copolymer **8** by human aortic endothelial cells: incubation time, 1 h (a), 3 h (b), 6 h (c), 24 h (d) (incubation at 37 °C), and 6 h (incubation at 4 °C) (e). Bars: 20 μm. The uptake is quantitatively represented as relative fluorescence intensity in the bar graph (f).

fluorescence intensity was normalized in a ratio of the fluorescence intensity at each incubation time to that at 1 h of incubation. The ratio was termed as the relative fluorescence intensity. The time course of the relative fluorescence intensity is shown in Figure 7f and indicates that HAECs incorporated progressively more nanoaggregates of **8** during the incubation time. The relative fluorescence intensity was 7-fold at 3 h, 11-fold at 6 h, and 76-fold at 24 h of incubation. In contrast, the relative fluorescence intensity dropped considerably and was only 12% of the control level (1 h at 37 °C) when HAECs were exposed to the nanoaggregates of **8** at 4 °C for 6 h. The fact that the temperature triggered a dramatic decrease in the relative fluorescence intensity suggests that the nanoag-

gregates are incorporated into HAECs by endocytosis. Endocytosis is known as a cellular process that is coupled with temperature-dependent metabolic activities.[18] Furthermore, it is known that some receptors and membrane microdomains of endothelial cell are involved in endocytosis.[19] However, it is not clear which of the endocytic pathways is responsible for the uptake of the nanoaggregates. This issue is now under investigation.

Conclusion

In this study, we investigated synthesis of the amphiphilic poly(*N*-propargylamide) **6** containing both sugar residues (hydrophilic part) and long alkyl chains (hydrophobic part) in order to develop a novel nanoaggregate based on the self-organization of amphiphilic polymers with rigid backbone. The desired polymer was prepared by copolymerization of the two *N*-propargylamide monomers **1** and **5** having a galactose residue and a lauryloyl group, respectively, catalyzed by a Rh complex. The GPC, ^{1}H NMR, SEM, and DLS analyses of the resulting copolymers indicated formation of the nanoparticles in water. The formation of the one-handed helical conformation of the copolymer in both DMSO and water was confirmed by the CD spectra. An amphiphilic poly(*N*-propargylamide) containing fluorescent dyes was newly designed to evaluate cell uptake of nanoparticles of the amphiphilic copolymer by fluorescence microscopy. The *N*-propargylamide monomer **7**, having a rhodamine B dye moiety, was prepared and copolymerized with **1** and **5**. Human aortic endothelial cells (HAECs) were cultured in a medium containing the fluorescent-dye-labeled amphiphilic copolymer. Cell uptake of the copolymer was confirmed by red fluorescence emission from each of the HAECs. Progressive uptake was observed during the incubation period. When the cell culture experiment was conducted at 4 °C, the fluorescence intensity of the red emission was considerably lowered. This indicates that the cell uptake is inhibited at 4 °C and that this uptake process should occur in an endocytic pathway rather than by simple adsorption to the plasma membrane of HAECs. We are now synthesizing a fluorescent-dye-labeled hydrophilic copolymer of monomer **1** with monomer **7** to study preferential cell uptake of the nanoaggregates of the amphiphilic copolymer. In the future, we anticipate that nanoparticles will be able to be preferentially endocytosed into cells rather than monomeric chains of water-soluble copolymer. If this does occur, the nanoparticles of the amphiphilic copolymer will be a promising nanocarrier for drug delivery.

Acknowledgements: This work was financially supported by the *Asahi Glass Foundation*. The author (T. N.) thanks Professor *Mitsuru Akashi* of Osaka University and Dr. *Takami Akagi* of the Japan Science and Technology Agency for dynamic light scattering measurement. The author (T. N.) thanks Dr. *Tetsuji Yamaoka* and Dr. *Atsushi Mahara* of the National Cardiovascular Center Research Institute for fluorescence spectroscopy analysis.

[1] M. Okada, *Prog. Polym. Sci.* **2001**, *26*, 67.
[2] Y. C. Lee, R. T. Lee, "*Neoglycoconjugates: Preparation and Applications*", Academic Press, San Diego **1994**.
[3] K. Kobayashi, A. Tsuchida, T. Usui, T. Akaike, *Macromolecules* **1997**, *30*, 2016.
[4] K. Kobayashi, N. Kakishita, M. Okada, T. Akaike, T. Usui, *J. Carbohydr. Chem.* **1994**, *13*, 753.
[5] L. L. Kiessling, N. L. Pohl, *Chem. Biol.* **1996**, *3*, 71.
[6] M.-G. Baek, R. C. Stevens, D. H. Charych, *Bioconjugate Chem.* **2000**, *11*, 777.
[7] I.-B. Kim, B. Erdogan, J. N. Wilson, U. H. F. Bunz, *Chem. Eur. J.* **2004**, *10*, 6247.
[8] T. Hasegawa, S. Kondoh, K. Matsuura, K. Kobayashi, *Macromolecules* **1999**, *32*, 6595.
[9] J. Kadokawa, Y. Shinmen, S. Shoda, *Macromol. Rapid Commun.* **2005**, *26*, 103.
[10] A. Takasu, K. Iso, T. Dohmae, T. Hirabayashi, *Biomacromolecules* **2006**, *7*, 411.
[11] K. Matsuura, S. Furuno, K. Kobayashi, *Chem. Lett.* **1998**, 847.
[12] J. Kadokawa, K. Tawa, M. Suenaga, Y. Kaneko, M. Tabata, *J. Macromol. Sci., Pure Appl. Chem.* **2006**, *43*, 1179.
[13] J. Deng, J. Tabei, M. Shiotsuki, F. Sanda, T. Masuda, *Macromolecules* **2004**, *37*, 9715 and references therein.
[14] R. R. Shrock, J. A. Osborn, *Inorg. Chem.* **1970**, *9*, 2339.
[15] J. Deng, J. Tabei, M. Shiotsuki, F. Sanda, T. Masuda, *Macromolecules* **2004**, *37*, 1891.
[16] M. Tabata, T. Sone, Y. Sadahiro, *Macromol. Chem. Phys.* **1999**, *200*, 265.
[17] J. Tabei, R. Nomura, T. Masuda, *Macromolecules* **2002**, *35*, 5405.
[18] G. Durin, S. Cottin, E. Blanc, A. R. Rees, *J. Tensamani. J. Biol. Chem.* **2003**, *278*, 31192.
[19] S. Muro, M. Koval, V. Muzykantov, *Curr. Vasc. Pharmacol.* **2004**, *2*, 281.

ELSEVIER

International Journal of Cardiology 111 (2006) 67 – 74

International Journal of Cardiology

www.elsevier.com/locate/ijcard

Postexercise VO_2 "Hump" phenomenon as an indicator for inducible myocardial ischemia in patients with acute anterior myocardial infarction

Hiroshi Takaki [a,*], Satoru Sakuragi [b], Noritoshi Nagaya [b], Shoji Suzuki [b], Yoichi Goto [b], Takayuki Sato [c], Kenji Sunagawa [a]

[a] *Department of Cardiovascular Dynamics, National Cardiovascular Center Research Institute, 5-7-1 Fujishiro-dai, Suita, Osaka, 565-8565, Japan*
[b] *Division of Cardiology, Department of Internal Medicine, National Cardiovascular Center, Suita, Japan*
[c] *Department of Cardiovascular Control, Kochi Medical School, Nankoku, Japan*

Received 13 October 2004; received in revised form 30 May 2005; accepted 24 July 2005
Available online 3 October 2005

Abstract

Objectives: At exercise testing with respiratory gas analysis in patients with inducible myocardial ischemia, we have occasionally observed abnormal transient oxygen uptake (VO_2) components with a characteristic "Hump"-shaped morphology early after exercise, which may serve as an index for inducible ischemia. We examined this hypothesis in patients with anterior q-wave myocardial infarction in whom the accuracy to identify ischemia by exercise ECG is limited.

Design: From patients with acute anterior q-wave infarction but without clinically overt heart failure who underwent pre-discharge exercise testing, we examined patients with (Group-I, $n=30$) and without (Group-N, $n=29$) inducible ischemia. To identify "Hump", postexercise VO_2 (up to 4 min) standardized for peak VO_2 was exponentially fitted with use of peak VO_2 and VO_2 of 90–240 s, yielding "expected VO_2". "D-curve" was obtained by subtracting "expected VO_2" from measured VO_2.

Results: Although exercise-induced ST depressions more frequently appeared in Group-I (27%) than in Group-N (3%, $p<0.05$), the prevalence was low. D-curve peaked later ($p<0.01$) and its value was greater ($p<0.05$) in Group-I than in Group-N. When "Hump" was defined to be present if D-curve peaked ≥ 40 s and its peak value $\geq 15\%$, it was far more frequently found in Group-I ($n=17/30$) than in Group-N ($n=1/29$, $p<0.01$). Thus, "Hump" could diagnose inducible ischemia with a sensitivity of 57% and a specificity of 97%.

Conclusions: Although not highly sensitive, postexercise VO_2 "Hump" with its peak occurring around 60 s after exercise is a specific marker for inducible ischemia. The identification may be useful, particularly in patients with limited accuracy of exercise ECG such as those with q-wave anterior infarction.

Keywords: Exercise test; Respiratory gas analysis; Myocardial ischemia; Oxygen uptake

1. Introduction

In patients after acute myocardial infarction, the evaluation of inducible myocardial ischemia is important in the subsequent management, [1–3]] however, the diagnostic accuracy of exercise ECG is known to be limited in those patients [4–8]]. This is particularly crucial in patients with q-wave anterior infarction, in whom exercise-induced ST-segment depression would be often obscured by the presence of q-wave in the precordial leads.

Exercise testing with respiratory gas analysis is most often performed for evaluating the functional capacity and predicting prognosis in patients with heart failure, however, we have conducted the test in a considerable number of these post-infarct patients (approximately 200 tests/year) in our institute for more than 10 years [9]. Although the concomitant use of respiratory gas analysis is conducted mainly for the same purpose as above, postexercise oxygen uptake (VO_2) kinetics may provide useful information for detecting inducible ischemia in these patients. In practice,

* Corresponding author. Tel.: +81 6 6833 5012; fax: +81 6 6835 5403.
E-mail address: htakaki@res.ncvc.go.jp (H. Takaki).

0167-5273/$ - see front matter
doi:10.1016/j.ijcard.2005.07.012

we have occasionally observed abnormal components with a characteristic "Hump"-shaped morphology in the early portion of the postexercise VO_2 decay in some of patients with evidence of inducible ischemia. The mechanism is unclear, however, it is conceivable that this phenomenon may be caused by enhanced stroke volume following resolution of ischemia during exercise, that is presumably responsible for delayed recovery of postexercise systolic blood pressure in patients with ischemia [10–15].

Abnormal VO_2 kinetics after exercise has been reported in patients with heart failure due to left ventricular dysfunction [16–18]. However, to our knowledge, no studies have examined the significance of the abnormal VO_2 kinetics after exercise occurring in association with inducible ischemia. We thus examined the diagnostic utility of this phenomenon ("Hump") as an indicator for inducible ischemia in patients after acute anterior q-wave infarction without clinically overt heart failure.

Table 1
Patients' characteristics

	Group-I (N=30)	Group-N (N=29)	p value
Sex (M/F)	26/4	22/7	NS
Age (years)	64±8	61±10	NS
LV EF (%)	39±7	43±9	NS
History of prior MI	7(23%)	2(7%)	NS
PCI therapy	13(43%)	24(83%)	<0.01
Coronary artery disease			
SVD	22(73%)		
DVD	5(17%)		
TVD	3(10%)		
Medication			
beta-blocker	13(43%)	6(21%)	NS
Ca antagonist	15(50%)	18(62%)	NS
Nitrate	21(70%)	10(34%)	<0.05
Digitalis	0 (0%)	2(7%)	NS

Values are expressed as mean±SD.
LVEF, left ventricular ejection fraction; MI, myocardial infarction; PCI, percutaneous coronary intervention; SVD, single vessel disease; DVD, double vessel disease; TVD, triple vessel disease.

2. Methods

2.1. Study population

From the consecutive inpatients with acute anterior q-wave myocardial infarction but without overt heart failure who underwent both pre-discharge exercise testing with respiratory gas analysis (within 3 weeks after the onset of infarction) and coronary angiography (approximately 4 weeks after the onset), we recruited the study population as follows. As a control group, we selected 29 patients (Group-N) who had no significant (>50% luminal diameter narrowing) stenosis in the coronary arteries at angiography, although 83% (n=24/29) of these patients had received percutaneous coronary intervention (PCI) during the acute phase of their infarction. It was assumed that this group did not have inducible ischemia. In 30 patients with abnormal coronary arteries, exercise thallium-201 scintigraphy (single-photon emission computed tomography; SPECT) showed reversible perfusion defects corresponding to the anatomic lesions demonstrated (Group-I). Of these patients, 43% (n=13/30) had received PCI during the acute phase, and at subsequent angiography 22 were left with single, five with double, and three with triple vessel disease (Table 1). All patients with Group-I subsequently received revascularization with either percutaneous transluminal angioplasty (n=26) or coronary artery bypass graft surgery (n=4).

We excluded patients with primary lung disease, orthopedic difficulties that precluded maximal exercise, arteriosclerotic obliterance and significant arrhythymias including atrial fibrillation. The patients with VO_2 plateau or leveling off (defined as an increase in VO_2 of less than 50 ml/min) around at peak exercise were also excluded (n=2), because the present study aimed to evaluate the significance of abnormal VO_2 kinetics ("Hump") only seen in the recovery period.

Left ventricular ejection fraction (LVEF) was similar between the two groups (Table 1). There were no significant differences in sex, age, and history of prior myocardial infarction. The use of cardiovascular drugs was similar in the two groups except for nitrate, and it was neither altered nor withheld for the exercise test. All patients gave informed consent for the study.

2.2. Exercise testing

Symptom-limited exercise testing with respiratory gas analysis was performed on an upright bicycle ergometer in a ramp fashion. After a 2-min rest, exercise was begun with a 1-min warm up at 0 W at 60 rpm, followed by 15 W incremental loading every 1 min. ECGs (V_1, V_5, aV_F) and heart rate (HR) were monitored throughout the testing, while recording hardcopies of 12-lead ECG every 1 or 2 min. HR and blood pressure (BP) measured by a conventional cuff sphygmomanometer were recorded at rest, at 1-min intervals during exercise, and 1, 2, and 4 min into the recovery period. All patients stopped exercise because of dyspnea and/or leg fatigue, and there was no patient in whom exercise was stopped because of angina, marked ST-segment depressions or fall of blood pressure. Patients were asked to stop pedaling soon after exercise (up to 10 s) to avoid the possible influence of cool-down exercise on recovery VO_2 kinetics.

Expired gas was measured on a breath-by-breath basis at rest, during the exercise, and recovery period (at least up to 4 min) with a respiromonitor AE280 (Minato Medical Electronics, Osaka, Japan). The system was carefully calibrated before each study. VO_2, carbon dioxide production (VCO_2), and minute ventilation (VE) were stored in a computer hard disk every 6 s for later analysis.

We identified a significant ST-segment depression induced by exercise according to the following criteria; (1) a horizontal or downsloping ST-segment displacement at J-point $\geq$0.1 mV (2) up-sloping ST-segment displacement at 80 ms after the J-point $\geq$0.15 mV in at least 3 consecutive beats at peak exercise. A significant ST-segment elevation was defined as an upward shift of the ST-segment $\geq$0.1 mV at the J-point compared with the resting level.

2.3. Exercise SPECT

The test was performed with symptom-limited bicycle exercise. At near-maximal exercise, thallium-201 was intravenously injected and the patient was encouraged to exercise for another 1 min. SPECT images were obtained at 15 min (initial images) and 4 h (delayed images). The images were assessed by two experienced physicians unaware of the patient clinical information. Thallium uptake was classified as normal, mildly, moderately or severely reduced, or absent. A reversible defect was defined when the classification improved by at least one category from the initial to delayed image.

2.4. Data analysis

By using our custom-made software, we evaluated abnormal manifestations ("Hump") in early postexercise VO_2 decay (Fig. 1). To characterize "Hump", we performed the following procedures, assuming that postexercise VO_2 decay would normally (i.e., without inducible ischemia) follow an approximately exponential curve and that "Hump" would be expressed by the components that was not fitted by this approximation. We first standardized the time-series of VO_2 data following exercise up to 4 min for peak VO_2. The curve was monoexponentially fitted with use of peak VO_2 and continuous VO_2 data over the period of 90–240 s; i.e., the data from 6 to 90 s were excluded from the fitting because we had observed abnormal components in this period. Nonlinear least-squares fitting was made assuming a monoexponential model: $y=Z_0\times e^{-t/\mu}+Z_\infty$ (where y is the standardized VO_2 data, Z_0 is the initial standardized VO_2 above Z_∞, μ is the time constant, t is time after the termination of exercise and Z_∞ is the asymptote to which standardized VO_2 decay).

The fitted curve was termed the "expected VO_2 curve" in this study (Fig. 1). To characterize "Hump" phenomenon, we obtained the "D-curve" by subtracting the expected VO_2 curve from actually measured VO_2 curve. In the D-curve that was a function of time (every 6 s) after exercise, we determined the peak value (D_{max}) in amplitude and the elapsed time at the time point of D_{max} (T_{max}). These two indices were compared between the two groups.

Systolic BP and HR at rest, at peak exercise and at the recovery period of 1, 2, and 4 min after exercise were also analyzed.

2.5. Statistical analysis

Values are expressed as mean±SD. Between-group differences for unpaired values were analyzed by Student's t test and by the Mann–Whitney U test when appropriate. Repeated measures of analysis of variance were used to

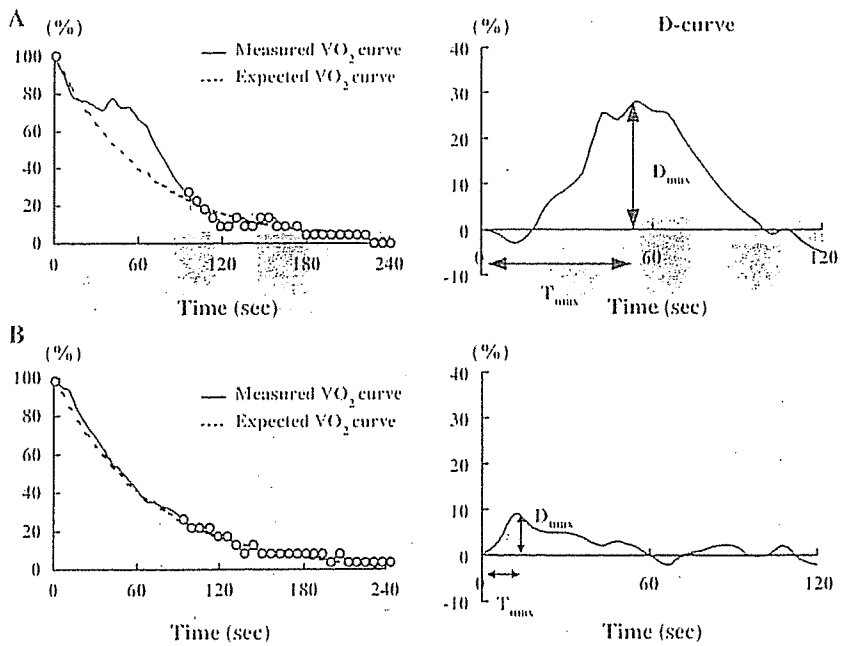

Fig. 1. Representative examples of postexercise VO_2 decay (left panel) and the derived D-curve (right panel) of two patients. Illustrated in the upper panels (A) are graphs for a patient of Group-I, and the lower (B) depict those for a patient of Group-N. After VO_2 decay curve standardized for peak VO_2 was exponentially fitted with use of peak VO_2 and VO_2 over the period of 90–240 s ("expected VO_2 curve", broken line), we obtained D-curve by subtracting "expected VO_2 curve" from actually measured VO_2 curve. In the D-curve, D_{max} (peak value) and T_{max} (time to peak) were estimated. VO_2 = oxygen uptake.

Table 2
Exercise variables

	Group-I ($N=30$)	Group-N ($N=29$)	p-value
Rest HR (bpm)	70±12	75±17	NS
Rest SBP (mm Hg)	128±26	119±16	NS
Duration of exercise (s)	510±66	553±87	<0.05
Exercise-induced angina	3(10%)	0(0%)	NS
Peak HR (bpm)	137±27	147±24	NS
Peak SBP (mm Hg)	174±25	178±25	NS
ECG change			
ST elevation	14(47%)	16(55%)	NS
ST depression	8(27%)	1(3%)	<0.05
Peak WR (watt)	113±19	123±22	NS
Peak VO_2 (ml/min)	1179±192	1335±278	<0.05

Values are expressed as mean±SD. HR, heart rate; SBP, systolic blood pressure; VO_2, oxygen uptake; WR, work rate.

compare the values during recovery period. When this test was significant, the Newman–Keuls post hoc test was performed for multiple comparisons. Difference in categorical variables was analyzed by chi-square analysis. A p-value ≤0.05 was considered statistically significant. Receiver operating characteristics curves (ROC) were used to assess the ability of T_{max} and D_{max} to diagnose inducible ischemia [19].

3. Results

3.1. Exercise testing results

Table 2 shows exercise parameters for Group-I and Group-N. There were no significant differences in rest HR, rest systolic BP (SBP), peak HR or peak SBP between the two groups. Although peak work rate was similar between the two groups, the duration of exercise was shorter and peak VO_2 was lower in Group-I than Group-N ($p<0.05$, both). However, these 2 parameters were of little help for differentiating the two groups; for instance, there was considerable overlap in peak VO_2 between the groups. Only 3 patients of Group-I complained of anginal symptoms after exercise.

As for ECG parameters, the frequency of a significant exercise-induced ST-segment elevation was comparable between Group-I and Group-N (47% and 55%, respectively). Despite the presence of inducible ischemia, a significant ST-segment depression was found in only 8 of 30 patients (27%) in Group-I, although it was more frequently observed in Group-I than in Group-N (27% vs. 3%, $p<0.05$).

3.2. Comparison of postexercise VO_2

To evaluate the overall difference in postexercise VO_2 decay (D-curve) between the 2 groups, we averaged the value of D-curve over every 30 s in the first 2 min of the recovery period (Fig. 2, upper two panels). As a result, the magnitude was significantly greater in the period of 30–60 s than in the period of 0–30 s in Group-I (13.7%±8.2% vs. 8.7%±5.1%, $p<0.01$, Fig. 2A), whereas such a difference was not observed in Group-N (11.0%±5.2% vs. 10.2%±5.0%, NS, Fig. 2B).

To characterize the "Hump" phenomenon in D-curve, the peak value (D_{max}) and its elapsed time (T_{max}) were compared between the groups. T_{max} was significantly longer in Group-I than in Group-N (42.6±14.6 vs. 31.2±13.2 s,

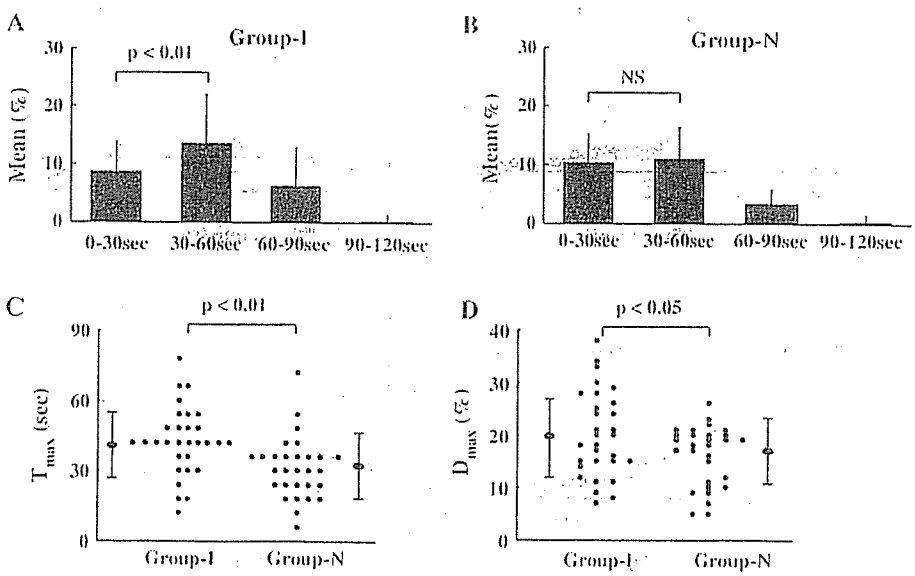

Fig. 2. The time-course changes in the D-curve for the first 2 min of recovery (upper panel) and comparisons of T_{max} (C, lower left panel) and D_{max} (D, lower right panel) between Group-I and Group-N. The D-curve values averaged over every 30 s were shown as bar graphs for Group-I (A, upper left panel) and Group-N (B, upper right panel). The mean for 30–60 s was greater than that for 0–30 s in Group-I ($p<0.01$), but not in Group-N. T_{max} was longer in Group-I than in Group-N ($p<0.01$), and D_{max} was greater in Group-I than in Group-N ($p<0.05$).

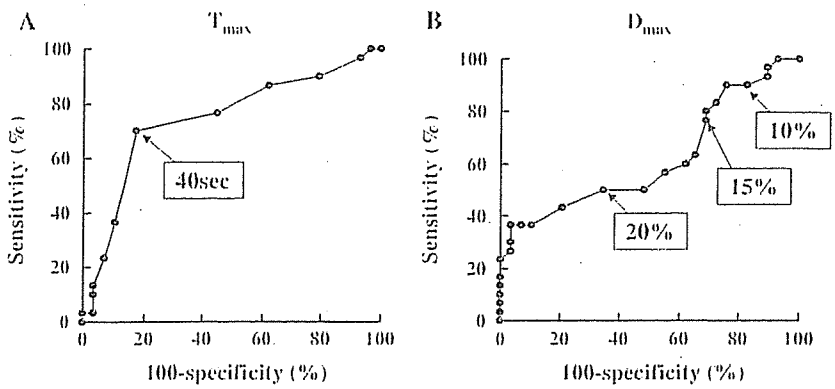

Fig. 3. ROC curves describing the ability for the diagnosis for inducible ischemia using T_{max} (A, left panel) and D_{max} (B, right panel).

$p<0.01$, Fig. 2C), and D_{max} was also significantly greater in Group-I than in Group-N (20.1%±8.1% vs. 16.2%±5.7%, $p<0.05$, Fig. 2D).

We used ROC analysis to determine the optimum cutoff values of these two parameters for identifying Hump phenomenon, i.e., inducible ischemia. When ROC analysis was conducted separately for T_{max} (Fig. 3A) and D_{max} (Fig. 3B), we could easily recognize 40 s as the optimum cutoff for T_{max} in differentiating the two groups, whereas such an optimum point was not found for D_{max}. Since it is considered that the combination of the two optimum cutoff values, each of which was determined by a separate ROC analysis, would not necessarily have the highest discriminative power, ROC analysis of T_{max} was repeated for a given D_{max}, while shifting D_{max} every 1% from 0% to 40%. As a result, when assuming that the best cutoff was defined as the point with highest sum of sensitivity and specificity, the combination of $D_{max} \geq 10\%$ and $T_{max} \geq 40$ s (from 37 to 41 s, because temporal resolution was 6 s) could most accurately discriminate Group-I from Group-N (sensitivity 67%, specificity 90%, accuracy 78%, Table 3). When $D_{max} \geq 15\%$ was applied (Fig. 4), the specificity was increased to 97%, although the sensitivity decreased to 57%.

3.3. Comparison of postexercise SBP

Although resting and peak SBP were not different between the two groups, Group-I had a higher SBP than Group-N at 2 and 4 min of recovery (both $p<0.05$, Fig. 5A).

Furthermore, among patients of Group-I, patients with "Hump", defined as $T_{max} \geq 40$ s and $D_{max} \geq 15\%$, had a higher SBP at 1 and 2 min of recovery than those without "Hump" (both $p<0.05$, Fig. 5B). A significant decrease in SBP from peak exercise was found at 1 min of recovery in patients without "Hump", but not in those with "Hump".

Table 3
Diagnostic accuracy of "Hump" for identifying inducible ischemia (Group-I)

T_{max} (s)	≥40	≥40	≥40
D_{max} (%)	≥10	≥15	≥20
Sensitivity	67% (20/30)	57% (17/30)	37% (11/30)
Specificity	90% (26/29)	97% (28/29)	100% (29/29)
Accuracy	78%	76%	68%

4. Discussion

Although exercise-induced ST-segment depression is a cardinal index to identify inducible myocardial ischemia on exercise testing, the diagnostic accuracy by the standard ST criteria is limited in post-infarct patients [4–8]. In our population consisting of patients after acute anterior q-wave myocardial infarction, ST-segment depressions during exercise appeared in only 27% of patients with inducible myocardial ischemia (Group-I), that was comparable to the incidence of ST depression reported previously [6–8]. The most likely explanation for the low sensitivity of ST depression in these patients is that exercise-induced ST elevation over q-wave leads, related to left ventricular asynergy, would mask the appearance of ST depression [5,20]. In patients with anterior q-wave myocardial infarction, the vector of ST-segment depression, which most frequently appears in the left precordial leads of V_4 to V_6,

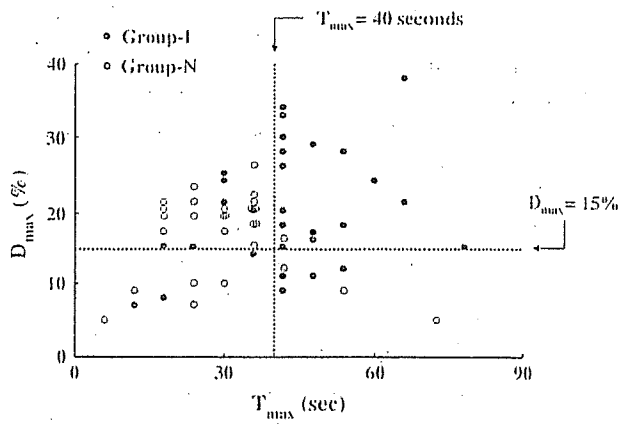

Fig. 4. Scatterplots showing D_{max} plotted against T_{max} for each patient. Approximately half (57%) of patients of Group-I (closed circle) were distributed in the limited area of $T_{max} \geq 40$ s and $D_{max} \geq 15\%$, whereas only one patient in Group-I (open circle) was distributed in this area. Using this criterion, we could diagnose the presence of inducible ischemia (Group-I) with a sensitivity of 57% and a specificity of 97%.

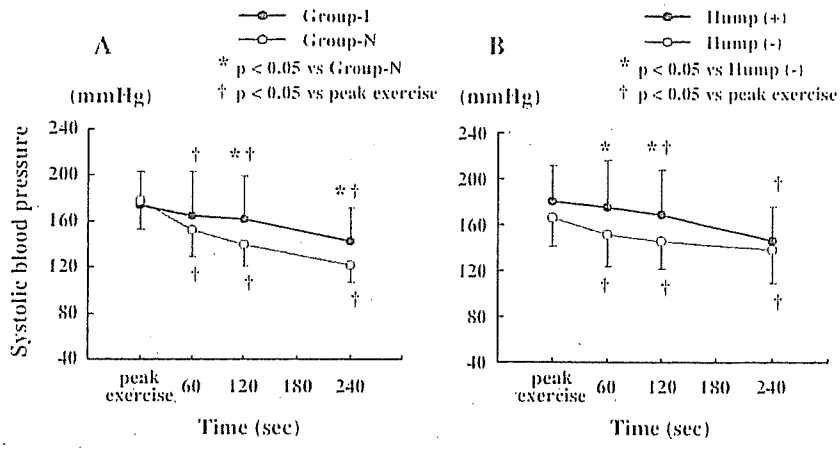

Fig. 5. Comparisons of systolic blood pressure time-course after exercise between Group-I and Group-N (A, left panel), and between the Group-I patients with and without "Hump" phenomenon (B, right panel).

may be electrically canceled by the opposite vector of ST elevation occurring in association with ventricular asynergy.

It is generally accepted that exercise-induced ST-segment elevation over post-infarct q-wave leads occurs in association with severe left ventricular asynergy, however, several studies indicated that exercise-induced ST-segment elevation might occur due to induced ischemia [21,22]. In the present study, we observed a similar prevalence of ST-segment elevation of ≥ 0.1 mV in Group-N (55%) and Group-I (47%, NS), suggesting that this index alone is of no use for identifying ischemia. We cannot exclude the possibility that ST-segment elevation might be caused by ischemia in some patients of Group-I, because three Group-I patients presented both exercise-induced ST-segment elevation and depression.

On the other hand, the present study has shown that abnormal transient VO_2 components after exercise, "Hump" phenomenon defined by our method described above, is a useful indicator for inducible ischemia in patients with acute anterior infarction. When the combination of $T_{max} \geq 40$ s and $D_{max} \geq 15\%$ were used for the definition of "Hump", we could diagnose inducible ischemia with sensitivity of 57%, specificity of 97%.

Abnormal postexercise VO_2 kinetics has been reported previously in patients with cardiocirculatory disorders. Hayasida et al. and other authors reported that the recovery of VO_2 was prolonged in patients with left ventricular dysfunction and that the time-course of VO_2 decay after exercise was closely related to exercise capacity [16–18,23–27] and prognosis [28]. Delayed energy store recovery in the skeletal muscle [22,24] and prolonged decrease in cardiac output [23,25–27,29] are considered to be involved in the genesis of this abnormal VO_2 recovery.

To our knowledge, there have been no published studies specifically examining the significance of exercise-induced ischemia on the postexercise abnormal VO_2 kinetics. Abnormal components of our interest; i.e., "Hump", is characterized by a transient convex bulge in the limited portion of VO_2 decay at around 1 min. The occurrence seems to appear not immediately but soon after the termination of exercise, generally lasting approximately 1 min. Previous reports estimated abnormal VO_2 kinetics by estimating the whole VO_2 decay with use of temporal parameters such as half time, [18,24,26] time constant [16,23,25] or cumulative area [28]. Since these measures are clearly unsuitable for our purpose, the non-exponential components (i.e., D-curve), that were derived by subtraction assuming that the abnormal components would be superimposed upon the monoexponential VO_2 decay, were compared between Group-I and Group-N. As a result, in Group-I, the mean value averaged over 30–60 s was greater than that averaged over 0–30 s, whereas such a difference was not found in Group-N (Fig. 2, upper two panels). Furthermore, the D-curve peaked later and its maximal value was greater in Group-I compared with Group-N (Fig. 2, lower two panels). Thus, the group difference of the D-curve with respect to the amplitude and temporal profile enabled us to identify the presence of inducible ischemia by the criterion shown in Table 3.

It was somewhat unexpected that some of patients without inducible ischemia (Group-N) showed a sizable amount of non-exponential components in the very early period of recovery up to 30 to 40 s. Our expectation was that non-exponential components in Group-N would be negligibly small, because the VO_2 decay curve should be closely fitted by the monoexponential model. This discrepancy indicates that postexercise VO_2 decay is not necessarily monoexponential in shape, and may be more precisely fitted by other mathematical models such as a sigmoidal model, even in the absence of inducible ischemia, although simple noise inherent in the measurements might be also related to the components. Impairment of LV function due to infarction and peripheral dysfunction caused by the immobilization (deconditioning effects) in the acute phase of myocardial infarction would contribute to the loss of the rapid fall of VO_2 immediately after exercise.

Several studies indicated that, in patients with inducible myocardial ischemia, an abnormal systolic blood pressure

response is observed not only during exercise but also during the recovery phase; a lesser decrease in systolic BP in the early recovery period, [10–15] which was in agreement with our results that the prolonged time-course of the postexercise decrease in systolic BP was seen in Group-I. It was also reported that, in these patients, stroke volume during exercise progressively decreased according to the development of severe ischemia, and it did not decrease but rather increased during the early period of recovery. [29–31] Although this paradoxical increase following exercise may occur either by a decrease in peripheral vascular tone after exercise [29,30] or by an improvement of LV function following the resolution of induced ischemia, [31] dynamic changes in the former factor are unlikely to transiently occur. The fact that, in Group-I, systolic BP at 1 min of recovery did not significantly decrease from peak exercise only in patients with "Hump", but not in patients without "Hump" reasonably suggests the direct role of enhanced stroke volume soon after exercise on the occurrence of "Hump".

The exact mechanism responsible for "Hump" is speculative, however, a recent study by Belardinelli et al. may provide a clue to the mechanism [32]. They indicated that exercise-induced ischemia resulting in a reduction in stroke volume decreases the increase rate of VO_2 to work rate increase (i.e., $\Delta VO_2/\Delta WR$) after the ischemic threshold. This reduction in $\Delta VO_2/\Delta WR$ would produce some amount of abnormal oxygen deficit (that is, extra-oxygen deficit), which might be paid back soon after exercise when the cardiac performance recovers. We consider that this process may be "Hump", transiently appearing on the limited portion of the early recovery of VO_2 decay. It should be noted that a reduction in $\Delta VO_2/\Delta WR$ during exercise was difficult to discern by visual inspection in any patient in our patients including those manifesting "Hump", probably because of a large spontaneous variations in VO_2 during exercise.

As described previously, it is possible that a mono-exponential curve used for deriving the non-exponential components is not be the most appropriate model for identifying "Hump". No single model may be suitable for fitting of the postexercise VO_2 decay, because the morphology of postexercise VO_2 decay curve considerably varied between individuals, probably due to the varying extent of impairment of LV function and the status of conditioning. Nevertheless, our method could identify "Hump" with a reasonable sensitivity and high specificity. Further investigation is necessary to ascertain this issue.

In conclusion, postexercise VO_2 "Hump" phenomenon, with its peak occurring around 60 s after exercise, seems to be a useful marker for inducible myocardial ischemia. The identification of this phenomenon may be more useful, particularly in patients with limited diagnostic accuracy of exercise ECG such as those with anterior myocardial infarction.

Acknowledgments

This study was supported by Research Grants for Cardiovascular Diseases (11C-7) from the Ministry of Health and Welfare of Japan, by Grant-in-Aid for Scientific Research (C-11670730) from the Japan Society for the Promotion of Science, and by the Program for Promotion of Fundamental Studies in Health Science from the Organization for Pharmaceutical Safety and Research.

References

[1] Taylor GJ, Humphries JO, Mellitis ED, et al. Predictors of clinical course, coronary anatomy and left ventricular function after recovery from acute myocardial infarction. Circulation 1980;62:960–70.
[2] Sanz G, Castoner A, Betriu A, et al. Determinants of prognosis in survivors of myocardial infarction: a prospective clinical angiographic study. N Engl J Med 1982;306:1065–70.
[3] De Feyter PJ, van Eenige MJ, Dighton DH, et al. Prognostic value of exercise testing, coronary angiography and left ventriculography 6–8 weeks after myocardial infarction. Circulation 1982;66:527–36.
[4] Theroux P, Waters DD, Halpen C, et al. Prognostic value of exercise testing soon after myocardial infarction. N Engl J Med 1979;301: 341–5.
[5] Castellanet MJ, Greenberg PS, Ellestad MH. Comparison of ST-segment change on exercise testing with angiographic findings in patients with prior myocardial infarction. Am J Cardiol 1978;42: 29–35.
[6] Tilkemeier PL, Guiney TE, LaRaia PJ, et al. Prognostic value of predischarge low-level exercise thallium testing after thrombolytic treatment of acute myocardial infarction. Am J Cardiol 1990;66: 1203–7.
[7] Froelicher VF, Perdue ST, Atwood JE, et al. Exercise testing of patients recovering from myocardial infarction. Eur Probl Cardiol 1986;11:370–444.
[8] Haber HL, Beller GA, Watson DD, et al. Exercise thallium-201 scintigraphy after thrombolytic therapy with or without angiography for acute myocardial infarction. Am J Cardiol 1993;71:1257–61.
[9] Tomita T, Takaki H, Hara Y, et al. Attenuation of hypercapnic carbon dioxide chemosensitivity after postinfarction exercise training: possible contribution to the improvement in exercise hyperventilation. Heart 2003;9:404–10.
[10] Kato K, Saito F, Hatano K, et al. Prognostic value of abnormal postexercise systolic blood pressure response; prehospital discharge test after myocardial infarction in Japan. Am Heart J 1990;119: 264–71.
[11] Miyahara T, Yokota M, Iwase M, et al. Mechanism of abnormal postexercise systolic blood pressure response and its diagnostic value in patients with coronary artery disease. Am Heart J 1990;120:40–9.
[12] Tsuda M, Hatano K, Hayashi H, et al. Diagnostic value of postexercise systolic blood pressure response for detecting coronary artery disease in patients with or without hypertension. Am Heart J 1993;125:718–24.
[13] Abe K, Tsuda M, Hayashi H, et al. Diagnostic usefulness of postexercise systolic blood pressure response for detection of coronary artery disease in patients with electrocardiographic left ventricular hypertrophy. Am J Cardiol 1995;76:892–5.
[14] Hashimoto M, Okamoto M, Yamagata T, et al. Abnormal systolic blood pressure response during exercise recovery in patients with angina pectoris. J Am Coll Cardiol 1993;22:659–64.
[15] McHam SA, Marwick TH, Pashkow FJ, et al. Delayed systolic blood pressure recovery after graded exercise. J Am Coll Cardiol 1999; 34:754–9.

[16] Hayashida W, Kumada T, Kohno F, et al. Post-exercise oxygen uptake kinetics in patients with left ventricular dysfunction. Int J Cardiol 1993;38:63–72.
[17] Riley M, Stanford CF, Nicholls DP. Ventilatory and heart rate responses after exercise in chronic cardiac failure. Clin Sci (Lond) 1994;87:231–8.
[18] Cohen-Solal A, Laperche T, Morvan D, et al. Prolonged kinetics of recovery of oxygen consumption after maximal graded exercise in patients with chronic heart failure. Circulation 1995;91:2924–32.
[19] Hanley JA, McNeil BJ. A method of comparing the areas under receiver operating characteristic curves derived from the same cases. Radiology 1983;148:839–43.
[20] Manvi KM, Ellestd MH. Elevated ST segments with exercise in ventricular aneurysm. J Electrocardiol 1972;5:317–23.
[21] Miyakado H, Kato M, Noguchi N, et al. Exercise-induced ST-segment elevation-role of left ventricular wall motion abnormalities and coronary artery narrowing. Jpn Circ J 1995;59:725–35.
[22] Feyter PJ, Majid PA, Eenige MJ, Wardeh R, Wempe FN, Roos JP. Clinical significance of exercise-induced ST segment elevation. Correlative angiographic study in patients with ischemic heart disease. Br Heart J 1981;6:84–92.
[23] Kitaoka H, Takata J, Furuno T, et al. Delayed recovery of postexercise blood pressure in patients with chronic heart failure. Am J Cardiol 1997;79:1701–4.
[24] Cohen-Solal A, Czitrom D, Geneves M, et al. Delayed attainment of peak oxygen consumption after the end of exercise in patients with chronic heart failure. Int J Cardiol 1997;60:23–9.
[25] Pavia L, Myers J, Cesare R. Recovery kinetics of oxygen uptake and heart rate in patients with coronary artery disease and heart failure. Chest 1999;116:808–13.
[26] Tanabe Y, Takahashi M, Hosaka Y, et al. Prolonged recovery of cardiac output after maximal exercise in patients with chronic heart failure. J Am Coll Cardiol 2000;35:1228–36.
[27] Daida H, Allison TG, Johnson BD, et al. Further increase in oxygen uptake during early active recovery following maximal exercise in chronic heart failure. Chest 1996;109:47–51.
[28] Groote P, Millaire A, Decoulx E, et al. Kinetics of oxygen consumption during and after exercise in patients with dilated cardiomyopathy. New markers of exercise intolerance with clinical implications. J Am Coll Cardiol 1996;28:168–75.
[29] Koike A, Ito H, Doi M, et al. Beat-to-beat evaluation of cardiac function during recovery from upright bicycle exercise in patients with coronary artery disease. Am Heart J 1990;120:316–23.
[30] Plotnick GD, Becker LC, Fisher ML, et al. Changes in left ventricular function during recovery from upright bicycle exercise in normal persons and in patients with coronary artery disease. Am J Cardiol 1986;58:247–51.
[31] Schneider RM, Weintraub WS, Klein LW, et al. Rate of left ventricular functional recovery by radionuclide angiography after exercise in coronary artery disease. Am J Cardiol 1986;57:927–32.
[32] Belardinelli R, Lacalaprice F, Carle F, et al. Exercise-induced myocardial ischaemia detected by cardiopulmonary exercise testing. Eur Heart J 2003;24:1304–13.

The EMBO Journal (2006) 25, 2388–2396 | © 2006 European Molecular Biology Organization | All Rights Reserved 0261-4189/06
www.embojournal.org

THE EMBO JOURNAL

Crystal structures of VAP1 reveal ADAMs' MDC domain architecture and its unique C-shaped scaffold

Soichi Takeda[1,2,*], Tomoko Igarashi[1], Hidezo Mori[1] and Satohiko Araki[3]

[1]Department of Cardiac Physiology, National Cardiovascular Center Research Institute, Suita, Osaka, Japan, [2]Laboratory for Structural Biochemistry, Riken Harima Institute at SPring-8, Mikazuki, Sayo, Hyogo, Japan and [3]Sugashima Marine Biological Laboratory, Graduate School of Science, Nagoya University, Toba, Mie, Japan

ADAMs (a disintegrin and metalloproteinase) are sheddases possessing extracellular metalloproteinase/disintegrin/cysteine-rich (MDC) domains. ADAMs uniquely display both proteolytic and adhesive activities on the cell surface, however, most of their physiological targets and adhesion mechanisms remain unclear. Here for the first time, we reveal the ADAMs' MDC architecture and a potential target-binding site by solving crystal structures of VAP1, a snake venom homolog of mammalian ADAMs. The D-domain protrudes from the M-domain opposing the catalytic site and constituting a C-shaped arm with cores of Ca^{2+} ions. The disintegrin-loop, supposed to interact with integrins, is packed by the C-domain and inaccessible for protein binding. Instead, the hyper-variable region (HVR) in the C-domain, which has a novel fold stabilized by the strictly conserved disulfide bridges, constitutes a potential protein–protein adhesive interface. The HVR is located at the distal end of the arm and faces toward the catalytic site. The C-shaped structure implies interplay between the ADAMs' proteolytic and adhesive domains and suggests a molecular mechanism for ADAMs' target recognition for shedding.

The EMBO Journal (2006) 25, 2388–2396. doi:10.1038/sj.emboj.7601131; Published online 11 May 2006
Subject Categories: signal transduction; structural biology
Keywords: ADAM; MDC; protein–protein interaction shedding; snake venom metalloproteinase

Introduction

ADAMs (a disintegrin and metalloproteinase) or MDC (metalloproteinase/disintegrin/cysteine-rich) proteins comprise an emerging class of mammalian metalloproteinases with potential regulatory roles in cell–cell and cell–matrix adhesion and signalling (Becherer and Blobel, 2003; Seals and Courtneidge, 2003; White, 2003; Blobel, 2005). To date, over 30 ADAMs have been identified in a variety of species from fission yeast to human. Roughly, half of these are believed to function as active metalloproteinases and thus to constitute major membrane-bound sheddase that can proteolytically release cell-surface-protein ectodomains including growth factors and cytokines, their receptors and cell adhesion molecules. For example, ADAM17 (TACE, TNF-α converting enzyme) releases many cell-surface proteins including TNF-α precursor (Black *et al*, 1997; Moss *et al*, 1997) and ADAM10 (kuzbanian), which dictates lateral inhibition of *Drosophila* neurogenesis (Rooke *et al*, 1996), releases Notch ligand Delta (Qi *et al*, 1999) and Notch itself (Pan and Rubin, 1997). With regard to cellular interactions, fertilin α and β (ADAM1 and ADAM2, respectively) have been identified as sperm surface molecules essential for fertilization (Primakoff *et al*, 1987; Blobel *et al*, 1990, 1992) and meltrin α (ADAM12) is implicated in myogenesis (Yagami-Hiromasa *et al*, 1995). ADAMs have been associated with numerous diseases including arthritis, Alzheimer's disease, and cancer (Duffy *et al*, 2003; Moss and Bartsch, 2004). ADAM33 has been genetically linked with asthma (Van Eerdewegh *et al*, 2002). ADAMs uniquely display both proteolytic and adhesive activities on the cell surface, however, most of their physiological targets and the adhesion mechanisms remain unclear.

Disintegrins are small proteins (40–90 aa) isolated from snake venom typically with an Arg-Gly-Asp (RGD) recognition sequence on an extended loop (disintegrin-loop) that inhibit platelet aggregation via integrin binding (Huang *et al*, 1987; Calvete *et al*, 2005). ADAMs are unique among cell surface proteins in possessing a disintegrin (D-) domain and thus it has been suggested that integrins might be common receptors for ADAMs (Blobel *et al*, 1992; Evans, 2001; White, 2003). However, the RGD sequence in the ADAMs' disintegrin-loop is usually replaced by XXCD and therefore, its adhesive potential has been controversial. Both the ADAMs' D- and cysteine-rich (C-) domains are involved in the protein–protein interactions (Myles *et al*, 1994; Almeida *et al*, 1995; Zolkiewska, 1999; Iba *et al*, 2000; Gaultier *et al*, 2002; Smith *et al*, 2002), however, the details of the interactions have remained elusive. This is because high-resolution structures have been available only for isolated domains (Maskos *et al*, 1998; Orth *et al*, 2004; Janes *et al*, 2005) and no structural information has been available for the C-domain of the canonical ADAMs. To clarify the molecular mechanisms of target recognition for shedding by and of cellular adhesion via ADAMs, elucidation of the atomic structure of the ADAMs' MDC domains is indispensable.

To obtain structural data on an ADAM family member, we exploited the fact that hemorrhagic P-III snake venom metalloproteinases (SVMPs) share the ADAMs' MDC architecture (Jia *et al*, 1996; Evans, 2001; Fox and Serrano, 2005). Most ADAMs possess additionally, EGF-like, transmembrane and cytoplasmic domains and therefore are primarily membrane-associated, whereas SVMPs are secreted. Vascular apoptosis-inducing protein-1 (VAP1) is a disulfide-bridged

*Corresponding author. Department of Cardiac Physiology, National Cardiovascular Center Research Institute, Fujishirodai 5-7-1, Suita, Osaka, 565-8565, Japan. Tel.: +81 6 6833 5012 ext.2381; Fax: +81 6 6872 7485; E-mail: stakeda@ri.ncvc.go.jp

Received: 17 February 2006; accepted: 12 April 2006; published online: 11 May 2006

homodimer P-III SVMP isolated from *Crotalus atrox* venom (Masuda *et al*, 1998, 2000). VAP1's stability and intrinsic two-fold symmetry enabled us to solve the crystal structures at 2.5-Å resolution. The structure reveals the residues that are important for stabilizing the MDC architecture are strictly conserved throughout the primary structure among all the known ADAMs. Therefore, the present structure represents the general architecture of ADAMs' MDC domains and provides insights into the molecular mechanism of the ADAMs' target recognition.

Results

Structure determination

VAP1 yielded crystals readily, and initial phases were determined by molecular replacement method using the structure of P-I SVMP, acutolysin-C (1QUA) (Zhu *et al*, 1999) as a starting model. Although the initial model, with 99 identical residues out of 197, represented less than 50% of the total molecule, two distinct local noncrystallographic two-fold symmetry (NCS) operations (see below) allowed us to completely model the whole molecule. The native structures were determined from the crystals with two distinct space groups, $P2_12_12_1$ and $P4_12_12$, both at 2.5-Å resolution (Table I). Orthorhombic crystals were used for inhibitor soaking and the GM6001 ((3-(*N*-hydroxycarboxamido)-2-isobutyl-propanoyl-Trp-methylamide))-bound structure was determined at 3.0-Å resolution (Table I). In either crystal forms, the asymmetric unit contained one dimer molecule. The four monomers in the two crystal forms have almost identical structures, except for slight variations in their domain orientations, terminal residues, surface loops and active-site GM6001-binding region.

MDC architecture

The MDC architecture of VAP1 is shown in Figure 1A and B. The metalloproteinase (M-) domains in the dimer are related by NCS such that their active sites point in opposite directions and an intermolecular disulfide bridge is formed between symmetry-related Cys365 residues (Figure 1A). The M-domain is followed by a disintegrin (D-) domain that is further divided into D_s- and D_a-domains (see below). The D_s-domain protrudes from the M-domain close to the Ca^{2+}-binding site I (see below) opposing the catalytic site. The D-domain forms a C-shaped arm, together with the cysteine-rich (C-) domain, with its concave surface toward the M-domain. There are no direct interactions between the arm and the M-domain. Notably, the distal portion of the C-domain comes close to

Table I Data collection and refinement statistics

	Native (orthorhombic)	Native (tetragonal)	GM6001-bound
Data collection			
Space group	$P2_12_12_1$	$P4_12_12$	$P2_12_12_1$
Cell dimensions			
a, *b*, *c* (Å)	86.7, 93.3, 137.7	93.9,93.9,244.8	86.3, 91.4, 136.0
α, β, γ (deg)	90, 90, 90	90, 90, 90	90, 90, 90
Resolution (Å)	50–2.50 (2.59–2.50)	50–2.50 (2.59–2.50)	50–2.95 (3.06–2.95)
R_{merge}[a]	0.072 (0.369)	0.084 (0.380)	0.072 (0.367)
$I/\sigma I$	14.4 (2.9)	18.7 (7.1)	12.6 (4.3)
Completeness (%)	99.4 (98.8)	99.7 (99.6)	99.9 (99.4)
Redundancy	3.91	12.7	4.95
Refinement			
Resolution (Å)	50–2.50 (2.59–2.50)	50–2.50 (2.59–2.50)	50–2.95 (3.06–2.95)
No. of reflections	38874	38786	23295
R_{work}[b]/R_{free}[c]	0.212/0.258	0.229/0.269	0.208/0.264
No. of atoms			
Protein	6558	6513	6558
Zn^{2+}	2	2	2
Ca^{2+}	4	4	4
Co^{3+}	1		1
N-acetyl glucosamine	56	42	56
GM6001			56
Water	205	165	35
B-factors			
Protein	44.9	51.2	55.4
Zn^{2+}	40.9	41.6	46.4
Ca^{2+}	43.5	52.4	49.3
Co^{3+}	35.5		56.8
N-acetyl glucosamine	69.8	65.1	75.8
GM6001			78.6
Water	39.8	41.5	37.0
R.m.s deviations			
Bond lengths (Å)	0.0052	0.0080	0.0038
Bond angles (deg)	1.18	1.39	0.92

[a]$R_{merge} = \sum_{hkl}\sum_i|I_i(hkl) - \langle I\ (hlk)\rangle| \ / \ \sum_{hkl}\sum_i I_i(hkl)$, where $I_i(hkl)$ is the *i*th intensity measurement of reflection *hkl* and $\langle I(hlk)\rangle$ is its average.
[b]$R_{work} = \sum(||F_{obs}| - |F_{calc}||/\sum|F_{obs}|$.
[c]R_{free} = *R*-value for a randomly selected subset (5%) of the data that were not used for minimization of the crystallographic residual.
Highest resolution shell is shown in parenthesis.
For each data set, single crystal was used for measurement.

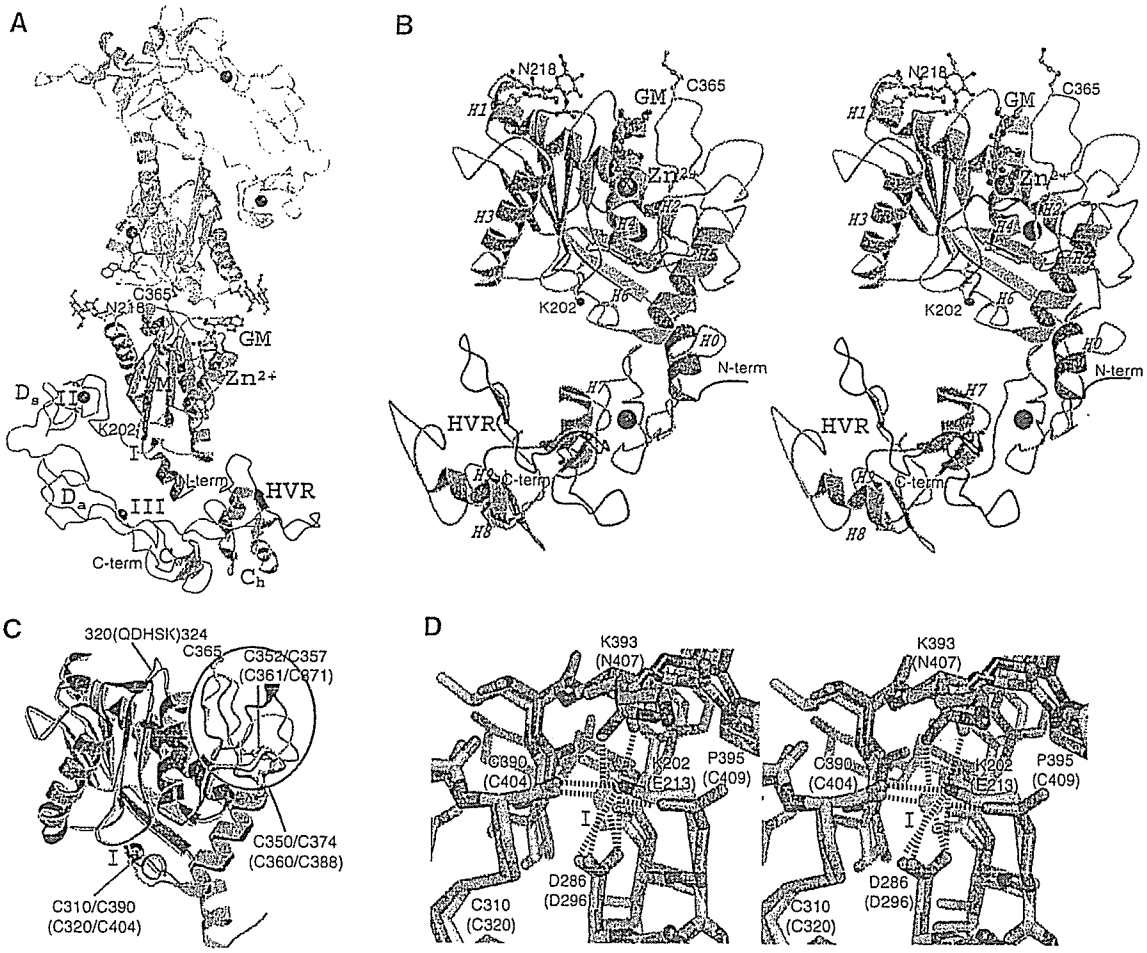

Figure 1 MDC architecture. (A) VAP1 dimer viewed from the NCS axis. The H0-helix, M-domain, linker, D_s-, D_a-, C_w-, and C_h-domains and HVRs belonging to the one monomer are shown in red, yellow, gray, cyan, pink, gray, green and blue, respectively. The disulfide-linked counterpart is shown in gray. Zinc and calcium ions are represented as red and black spheres, respectively. The NAG (*N*-acetyl-glucosamine, in orange) moieties linked to Asn218, the calcium-mimetic Lys202 and the bound inhibitor GM6001 (GM, in green) are in ball-stick representations. (B) Stereo view of VAP1 monomer from the direction nearly perpendicular to (A). The helix numbers are labelled. (C) Superposition of the M-domains of ADAM33 (blue) and VAP1 (yellow). The calcium ion bound to site I and the zinc ion in ADAM33 are represented by black and red spheres, respectively. The disulfide bridges are indicated in black and blue letters for VAP1 and ADAM33, respectively. The QDHSK sequence for the dimer interface in VAP1 (residues 320–324) is in red. (D) Comparison of the calcium-binding site I structures of ADAM33 (blue) and VAP1 (yellow) *in stereo*. The residues in ADAM33 and in VAP1 are labelled in blue and black, respectively. A calcium ion and a water molecule bound to ADAM33 are represented as green and red spheres, respectively. The ammonium group of Lys202 in VAP1 occupies the position of the calcium ion in ADAM33. In ADAM33 (Orth *et al*, 2004), side-chain oxygen atoms of Glu213, Asp296 and Asn407, the carbonyl oxygen of Cys404 and a water molecule form the corners of a pentagonal bipyramid and ligand to the calcium ion.

and faces toward the catalytic site in the M-domain. The C-terminus Tyr610 is located proximal to the boundary between the D_a- and C-domains (Figure 1A and B). Aside from Cys365, each monomer contains 34 cysteinyl residues, all of which are involved in disulfide bonding, and their spacings are strictly conserved among ADAMs (Figure 2 and Supplementary Figure 1) except within the substrate-binding (between the helices H4 and H5) and the HVR (see below) regions. Figure 2 provides a selected subset of the sequence alignments and the entire alignments of VAP1 and 39 ADAM sequences, including all 23 human ADAMs so far available, can be found as Supplementary Figure 1.

M-domain

Each VAP1 M-domain corresponds to a very similar structure to that of ADAM33 (Orth *et al*, 2004), with a flat ellipsoidal shape having a central core made up of five stranded β-sheets and five α-helices and a conserved methionine (Met-turn) below the active site histidine residues, which bears the typical structural feature of metzincin family of metalloproteinases (Bode *et al*, 1993). However, they differ in the dimer interface and the loop structure around the substrate-binding site (Figure 1C) that corresponds to the variable region in the primary structure (between the helices H4 and H5, see Figure 2). The N-terminal helix (H0) is also unique in VAP1. The dimer interface is best characterized by the recognition sequence QDHSK (residues 320–324, see Figure 1C and Supplementary Figure 2A–C) and by Cys365, however these are not conserved among ADAMs; therefore, none of the ADAMs' M-domains are suggested to form a stable dimer as VAP1. A peptide-like hydroxamate inhibitor GM6001 binds to VAP1 (Figure 1A and B, and Supplementary Figure 2D and E) in exactly the same manner as in the marimastat-ADAM33 M-domain complex (Orth *et al*, 2004), suggesting that the catalytic sites of VAP1 and ADAM33 share a common substrate recognition mechanism. The ADAM33

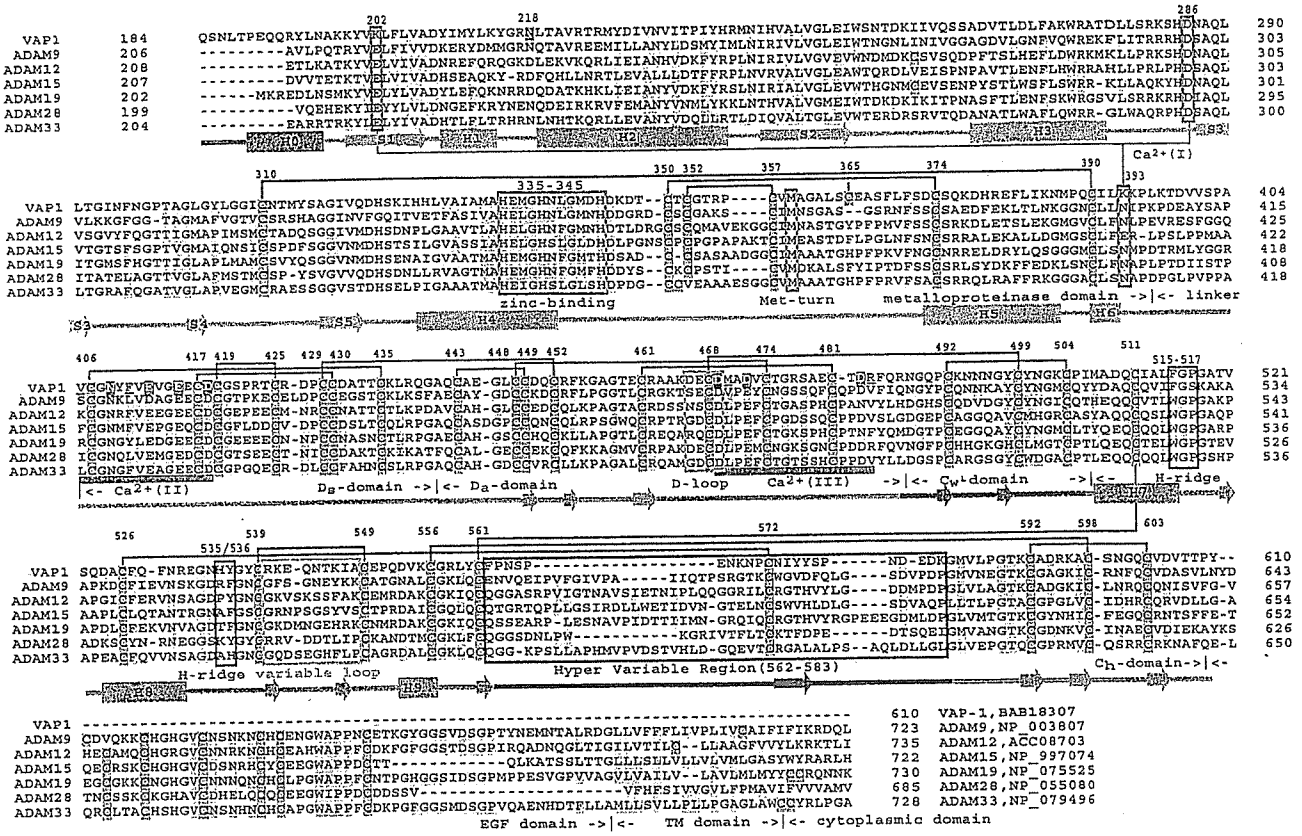

Figure 2 Sequence alignments of VAP1 and human ADAMs. The cysteinyl residues and the conserved residues are shaded in pink and yellow, respectively. Disulfide bridges, secondary structures and domains are drawn schematically. The HVR, calcium-binding site I, catalytic site and disintegrin-loop (D-loop) are boxed in blue, red, green and cyan, respectively. The hydrophobic ridges (H-ridges) are indicated. Calcium-binding sites II and III and the coordinating residues (shaded in red) are indicated. The NCBI accession numbers for the sequences are indicated.

M-domain structure suggests that most ADAMs have a Ca^{2+}-binding site (designated Ca^{2+}-binding site I) opposing the active-site cleft; however, in VAP1, the distal ammonium group of Lys202 substitutes for the Ca^{2+} ion (Figure 1D). Replacement of the calcium-coordinating glutamate residue with lysine also occurs in ADAM16, ADAM25 and ADAMs38–40 (Supplementary Figure 1).

C-shaped arm

The D-domain follows the M-domain, with a short linker that allows slightly variable domain orientations at V405 as a pivotal point (Figure 3C). The D-domain is further divided into two structural subdomains (Figure 3), the 'shoulder' (D_s-domain, residues 396–440) and the 'arm' (D_a-domain, residues 441–487). The D_s- and D_a-domains constitute a continuous C-shaped arm, together with the following N-terminus region of the C-domain which we designate the 'wrist' (C_w-domain, residues 488–505). There are three disulfide bonds in the D_s-domain, three in the D_a-domain and one in the C_w-domain. The subdomains are connected by single disulfide bridges (Figures 2 and 3A) with slightly variable angles (Figure 3B).

Both the D_s- and D_a-domains contain structural calcium-binding sites. In the D_s-domain, the side-chain oxygen atoms in residues Asn408, Glu412, Glu415 and Asp418, and the carbonyl oxygen atoms of Val405 and Phe410 are involved in pentagonal bipyramidal coordination and constitute Ca^{2+}-binding site II (Figures 2 and 3A). Notably, these residues are strictly conserved among all known ADAMs (Supplementary Figure 1). However, the side-chain oxygens of Asp469, Asp472 and Asp483, and carbonyl oxygens of Met470 and Arg484 form the corners of a pentagonal bipyramid to the calcium ligand and constitute the D_a-domain Ca^{2+}-binding site III (Figures 2 and 3A) and these residues are highly conserved among ADAMs except ADAM10 and ADAM17 (Supplementary Figure 1). Because of the few secondary-structural elements, bound calcium ions and the disulfide bridges are essential for the structural rigidity of ADAM's C-shaped arm. The RGD-containing disintegrin trimestatin (Fujii *et al*, 2003) has a similar structure with the D_a-domain (r.m.s.d of 1.24 Å, Figure 3B); however, no disintegrins have been shown to bind Ca^{2+} ions.

Using isolated D-domains or portions thereof, numerous ADAMs and P-III SVMPs have been shown to interact specifically with particular integrins (Evans, 2001; White, 2003; Calvete *et al*, 2005). However, the disintegrin-loop is packed against the C_w-domain and a disulfide bridge (Cys468–Cys499) further stabilizes the continuous structure (Figure 3A). Therefore, the disintegrin-loop is inaccessible for protein binding.

Hand domain

The 'hand' domain (C_h-domain, residues 505–610) follows the C_w-domain. The C_h-domain, together with the C_w-domain, constitutes a novel fold (Figure 4A). In either crystal form, VAP1 dimers interact with molecules of neighboring

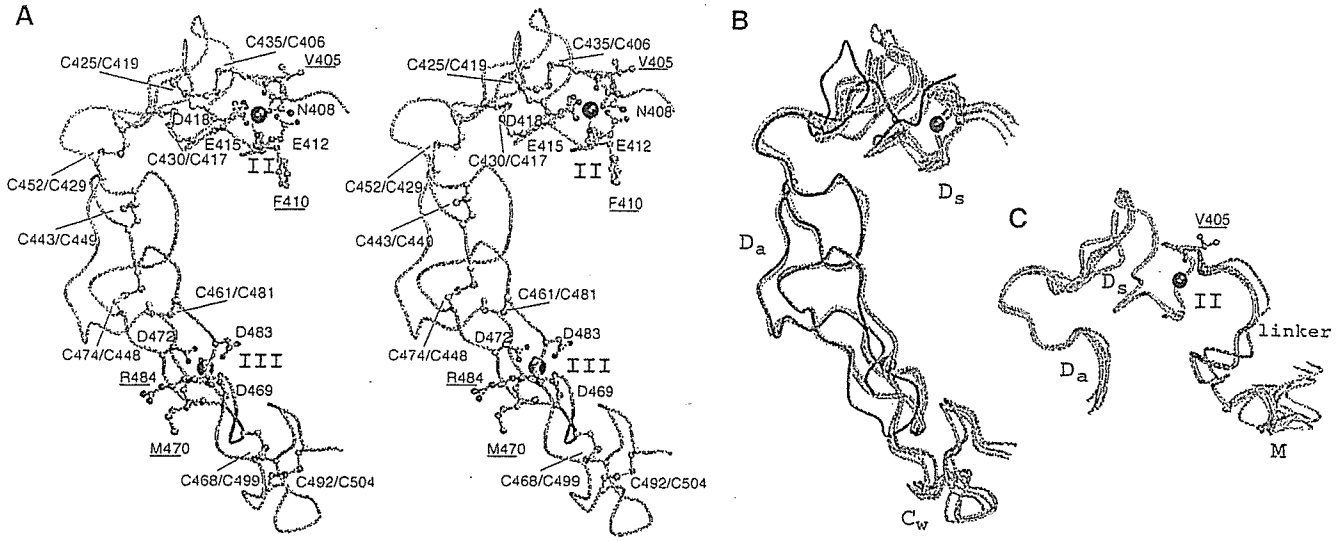

Figure 3 Arm structure. (A) Arm structure *in stereo*. The D_s-, D_a-, and C_w-domains are in cyan, pink and light green, respectively. The calcium-coordinating residues and the disulfide bridges are shown in red and green, respectively. The residues with carbonyl oxygen atoms involved in calcium coordination are underlined. Calcium ions are represented as black spheres. The disintegrin-loop (DECD) is in blue. (B) Superimposition of the four D_a-domains of VAP1 and trimestatin (1J2L). Trimestatin and its RGD loop are shown in red and blue, respectively. (C) Superimposition of the four D_s-domains. The linker between the M- and D_s-domains is shown in gray. Val405 at the pivotal point is indicated.

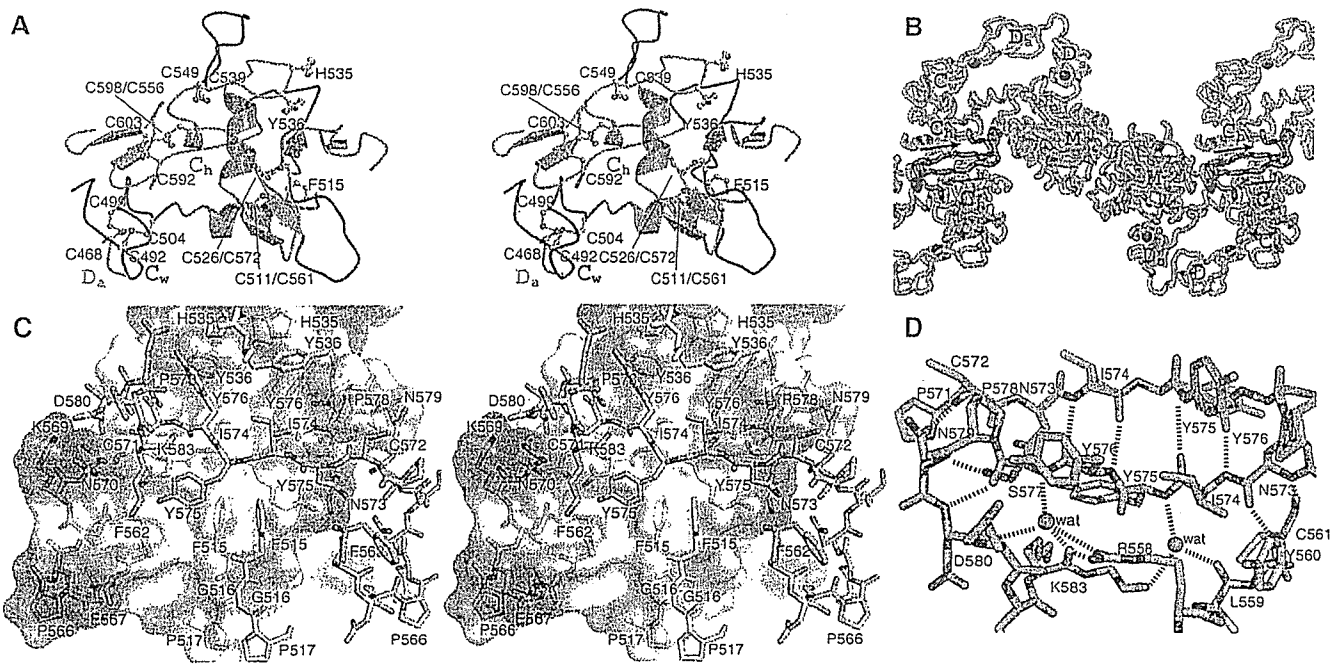

Figure 4 C-domain architecture and HVR. (A) The C-domain architecture *in stereo*. The C_w- and C_h-domains are in gray and light green, respectively. The disulfide bridges and the residues forming the hydrophobic ridges are indicated. The HVR and its NCS counterpart are shown in red and blue, respectively. The variable loop (residues 539–549), flanked by two adjacent cysteine residues, is in green. (B) Crystal packing in the orthorhombic crystal. The crystallographically equivalent molecules (HVRs) are in cyan (blue) and pink (red), respectively. The arrows indicate the directions of the HVR chains. Zinc and calcium ions are represented as red and black spheres, respectively. (C) Interactions between the HVRs (cyan and pink) *in stereo*. The molecular surface of the cyan molecule is shown with the electrochemical surface potential (red to blue). The residues constituting the hydrophobic ridges are in yellow. The residues are labelled in blue and red for cyan and pink, respectively. (D) Water-mediated hydrogen-bond network in the HVR. The HVR residues are in pink and cyan; non-HVR residues in the pink molecule are in gray.

units through the C_h-domains such that the molecules form a handshake (Figure 4B). Each C_h-domain interacts with its counterpart through a relatively large complementary surface of 860 Å^2 forming another NCS at the center, although VAP1 exists as dimers, not as oligomers, and is mono-dispersed in solution (data not shown).

HVR as a potential adhesive interface

C_h-domain residues 562–583 are predominantly involved in the handshake (Figure 4B). This is the region in which the ADAM sequences are most divergent and variable in length (16–55 aa) (Figure 2 and Supplementary Figure 1). We have designated this as the hyper-variable region (HVR). The HVR

is subdivided into two structural elements. The N-terminal portion (residues 562–572) fits into an extended loop, filling the gap between the M-domain and the neighboring molecule's C_h-domain and thus fixing the position of the arm (Figure 4B). The variable structures and less-specific interactions suggest that this loop is stabilized by crystal packing. Some ADAMs possess a putative fusion peptide in this segment typical of viral fusion proteins (Blobel *et al*, 1992; Yagami-Hiromasa *et al*, 1995), although their role in the actual fusion process has not been demonstrated. However, the remainder of the HVR (residues 572–583) interacts extensively with its counterpart by forming an antiparallel β strand at the center (Figure 4C and D). Although the ability to form β strand is predictable from the sequence, this β strand is stabilized mainly by interchain interactions (Figure 4D). There are no intrachain hydrogen bonds between residues 574–577 and the remainder of the C_h-domain; however a water-mediated hydrogen-bond network stabilizes this segment (Figure 4D). Therefore, it appears, that this β strand might be formed by the induced-fit mechanism upon the association of the C_h-domains and that the conserved disulfide bond (Cys526–Cys572, see Figure 4D) may stabilize the structure when the HVRs are isolated in solution. In addition to the main-chain hydrogen bonds, side-chain atoms (particularly residues I574, Y575, Y576 and P578) in the HVR β strand contribute numerous von der Waals interactions with their counterparts. Aside from the HVR, aromatic residues located at both sides of the β strand in close proximity to the NCS axis create additional interaction surfaces: residues Phe515, Gly516, His535 and Tyr536 in the loop regions form hydrophobic ridges that fit complementarily into the NCS region (Figure 4C). The hydrophobic ridges are highly conserved among ADAMs (Figure 2 and Supplementary Figure 1), thus, in part, they may also constitute binding surfaces.

Discussion

The VAP1 structures reveal highly conserved structural calcium-binding sites and the numbers and the spacings of cysteinyl residues that are essential for maintaining structural rigidity and spatial arrangement of the ADAMs' MDC domains. The C-shaped MDC architecture implies meaningful interplay between the domains and their potential roles in physiological functions.

The HVR creates a novel interaction interface in collaboration with the conserved hydrophobic ridges. Different ADAMs have distinct HVR sequences, which result in distinct surface features, thus, they may function in specifying binding proteins. The HVR is at the distal end of the C-shaped arm and points toward the M-domain catalytic site, with a distance of ~4 nm in between them. Collectively, these observations suggest that the HVR captures the target or associated protein that is processed by the catalytic site (Figure 5). The disintegrin portion is located opposit to and apart from the catalytic site and, thus, might play a primary role as a scaffold that allocates these two functional units spatially. The C-shaped structure also implies how the ADAMs' C-domains cooperate with their M-domains (Reddy *et al*, 2000; Smith *et al*, 2002). In membrane-bound ADAMs, the EGF-like domain (~60 aa) follows the C_h-domain (Figure 2) and presumably works as a rigid spacer connecting the MDC-domains with and orientating against the membrane-spanning region (Figure 5A). Many ADAMs are proteolytically inactive (because of the defects in the catalytic HEXXHXXGXXHD sequence or the post-translational removal of the M-domain), and several of these are important developmentally. Therefore, the HVR may also work to modulate cell–cell and cell–matrix interactions. There is some experimental evidence for C-domain-mediated adhesion. Peptides encompassing the HVR and the hydrophobic ridge from P-III SVMPs interfere with platelet interaction and collagen binding (Kamiguti *et al*, 2003). A recombinant atrolysin-A C-domain specifically binds collagen I and von Willebrand factor (vWF) and blocks collagen–vWF interaction (Jia *et al*, 2000; Serrano *et al*, 2005). ADAM12 interacts with cell-surface syndecan through its C-domain and mediates integrin-dependent cell spreading (Iba *et al*, 2000). The D/C-domain portion of ADAM13 binds to the ECM proteins laminin and fibronectin (Gaultier *et al*, 2002). However, most of these studies do not assign specific regions of the C-domain to these interactions and the molecular recognition mechanisms are to be elucidated.

ADAM10 and ADAM17 lack the Ca^{2+}-binding site III and show less sequence similarities in the C-domain with other

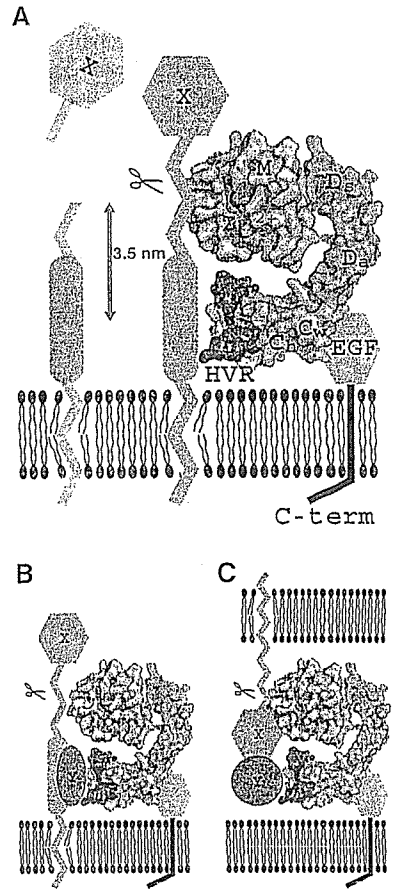

Figure 5 Models for ADAM's shedding. The molecular surface of the VAP1 monomer, without VAP1's unique H0-helix, are colored as in Figure 1A. Hydrophobic ridges are in yellow. EGF-like, transmembrane and cytoplasmic domains are represented schematically. (A) Membrane-anchored substrate molecule 'X' is directly recognized and captured by the HVR on the membrane-bound ADAM molecule. The distance between the center of the HVR (Tyr575) and the catalytic zinc ion is about 3.5 nm. (B) Substrate 'X' is recognized by the ADAM HVR via binding with an associated protein 'Y'. (C) ADAM cleaves substrate 'X' in *trans* via binding with an associated protein 'Y'.